ISPRS Journal of Photogrammetry and Remote Sensing 215 (2024) 112–135

Contents lists available at ScienceDirect

ISPRS Journal of Photogrammetry and Remote Sensing

journal homepage: www.elsevier.com/locate/isprsjprs

Improving PRISMA hyperspectral spatial resolution and geolocation by using Sentinel-2: development and test of an operational procedure in urban and rural areas

Giandomenico De Luca [a,*], Federico Carotenuto [a], Lorenzo Genesio [a], Monica Pepe [b], Piero Toscano [a], Mirco Boschetti [b], Franco Miglietta [a], Beniamino Gioli [a]

[a] Institute of BioEconomy (IBE), National Research Council of Italy (CNR), Via Madonna del Piano 10, 50145 Sesto Fiorentino, Italy
[b] Institute for Electromagnetic Sensing of the Environment (IREA), National Research Council of Italy (CNR), Via Bassini 15, 20133 Milano, Italy

ARTICLE INFO

Keywords:
Hyperspectral
Multispectral
Image fusion
Pansharpening
Co-registration
HySure
AROSICS

ABSTRACT

Hyperspectral (HS) satellites like PRISMA (*PRecursore IperSpettrale della Missione Applicativa*) offer remarkable capabilities, yet they are constrained by a relatively coarse spatial resolution, curbing their efficacy in those applications that require pinpoint accuracy. Here we propose a fusion process, aimed at the enhancement of PRISMA HS spatial resolution by using the spatial and spectral information of Sentinel-2 multispectral (MS) data (HS-MS fusion process), validated against four airborne HS flights simultaneous to satellite overpasses on different land use distributions. Adopting the PRISMA panchromatic (PAN) image, the proposed solution was also compared with the results of a HS-PAN pansharpening process. A two-steps operational workflow is proposed, based on two state-of-the-art and open-source algorithms. The first step consisted of the geocoding of PRISMA L2 products using Senintel-2 as reference and was accomplished with the phase-based algorithm implemented in AROSICS (Automated and Robust Open-Source Image Co-registration Software). The geometric displacement in L2 data was found to be between 80 m and 250 m, irregularly spatially distributed throughout the same scene and among scenes, and it was corrected by means of thousands of regularly spatially distributed tie points. A second-order polynomial transformation function was integrated in the algorithm. The second step consisted of employing the HySure (HS Super resolution) fusion algorithm to perform both the HS-MS fusion and the HS-PAN pansharpening, returning a PRISMA HS improved dataset with a spatial resolution of 10 m and 5 m, respectively. Four different per-band accuracy metrics were used to evaluate the accuracy of both products against airborne data. Overall, HS-MS data achieved increased accuracy in all validation metrics, i.e. + 28 % (root mean square error, RMSE), +23 % (spectral angle mapper, SAM), +7% (peak signal-to-noise ratio, PSNR) and + 11 % (universal image quality index, UIQI), with respect of HS-PAN data. These outcomes showed that using the spectral information of Sentinel-2 both spectral and spatial patterns were reconstructed more consistently in three different urban and rural scenarios, avoiding the presence of blur and at-edge artefacts as opposed to HS-PAN pansharpening, therefore suggesting an optimal strategy for satellite HS data resolution enhancement.

1. Introduction

Hyperspectral (HS) image systems, with high spectral resolutions, lead to more accurate characterisation of the Earth's surface and biosphere and assessment of its chemical and (bio)physical composition (Alicandro et al., 2022; Brezini and Deville, 2023; Lanaras et al., 2017; Vangi et al., 2021) with respect multispectral sensors (MS). In the context of spaceborne remote sensing, this finer spectral resolution has been exploited in several different Earth observation application domains, ranging from natural resources, semi-natural environments, and urban areas (Qian, 2021).

Among the last HS-related space missions, the PRISMA (*PRecursore IperSpettrale della Missione Applicativa*) (Loizzo et al., 2019), funded by the Italian Space Agency (ASI), opened new opportunities for the study and application of spaceborne HS information in Earth observation (Alicandro et al., 2022). It deploys an innovative optical instrument,

* Corresponding author.
E-mail address: giandomenicodeluca@cnr.it (G. De Luca).

https://doi.org/10.1016/j.isprsjprs.2024.07.003
Received 26 February 2024; Received in revised form 11 June 2024; Accepted 1 July 2024
Available online 8 July 2024
0924-2716/© 2024 The Author(s). Published by Elsevier B.V. on behalf of International Society for Photogrammetry and Remote Sensing, Inc. (ISPRS). This is an open access article under the CC BY license (http://creativecommons.org/licenses/by/4.0/).

which comprises a HS sensor based on a prism spectrometer, in combination with a panchromatic (PAN) camera. PRISMA was launched in March 2019 as precursor for future developments and releases (expected operating life of 5 years), with the purpose to assess the HS capability for monitoring Earth's natural resources, ecosystems and atmosphere. The free-data-access to PRISMA data has been enabled since May 2020, while, (Cogliati et al., 2021; Guarini et al., 2018; Loizzo et al., 2019; Pignatti et al., 2022, 2013) an independent scientific CAL/VAL activity was made since 2019 by the PRISCAV project (PRISMA CAL/VAL), investigating the performance of the sensors over a set of selected areas covering different land-uses (Cogliati et al., 2021; Guarini et al., 2018; Loizzo et al., 2019; Pignatti et al., 2022, Pignatti et al. (2013)). Further scientific contributes have already been shared with the community, focusing non-photosynthetic vegetation detection and classification (Pepe et al. 2020; 2023), soil matter characterization (Angelopoulou et al., 2023), water bodies investigation (Amieva et al., 2023; Giardino et al., 2020; Niroumand-Jadidi et al., 2020), marine plastic litter detection (Kremezi et al., 2021), methane point sources assessment (Guanter et al., 2021), archaeology (Alicandro et al., 2022), fire severity mapping (Quintano et al., 2023), cryosphere (Bohn et al., 2022; De Gregorio et al., 2023) urban local climate zones classification (Vavassori et al., 2023), highlighting an increasing interest of diverse communities around these HS data.

To achieve an acceptable signal-to-noise ratio (SNR) (Wang et al., 2021; Zhang et al., 2023), the ground sampling distance (GSD) of PRISMA HS images is limited at 30 m x 30 m. Such trade-off prevents the applications to those frameworks requiring a spatial detailed analysis (Acito et al., 2022; Brezini and Deville, 2023; Niroumand-Jadidi et al., 2020).

The spatial resolution improvement of optical satellite imagery is a common issue in Earth observation frameworks, therefore largely addressed in the literature (Brezini and Deville, 2023; Dian et al., 2021; Vivone, 2023). Several applications may benefit from the improvement of spatial resolution, where it is necessary to distinguish specific spatial features in agricultural, lithological, glacier and urban contexts (Acito et al., 2022; Brezini and Deville, 2023; Kremezi et al., 2021; Niroumand-Jadidi et al., 2020), or classification tasks (Lanaras et al., 2017; Vangi et al., 2021). More generally, an increase in spatial resolution would also improve multi-sensor interoperability, combining HS and higher resolution MS sensors. Alicandro et al. (2022), for example, expressed the possibility of a substantial archaeological multiscale analysis improvement if robust pansharpening method would be developed for spatial resolution enhancement of PRISMA HS data.

Pansharpening and image fusion represent the most common and effective approaches to enhance the spatial resolution of HS data (Dian et al., 2021; Vivone, 2023; Wang et al., 2021). The pansharpening technique (HS-PAN pansharpening) refers to the process of HS image spatial resolution improvement by exploiting the high-resolution geometric detail provided by a single-band panchromatic (PAN) visible image; that is why spaceborne HS sensors, including PRISMA, often acquire a synchronous high-resolution PAN image. Pansharpening methods were the first to be applied, relying on the established use of this technique to improve the spatial resolution of MS images (Vivone et al., 2021). However, due to the significant gap between the spectral range covered by the PAN's and HS's spectra, the pansharpening approach generally returns both spectral and spatial distortions (Brezini and Deville, 2023; Dian et al., 2018).

As an extension of pansharpening, the image fusion (HS-MS fusion) of a HS image with a MS image is based on exploiting the spatial information (finer than HS) and spectral information (finer than PAN) of MS data for HS spatial resolution improvement, preserving the consistency with the original HS spectral information (Brezini and Deville, 2023; Dian et al., 2021; Lanaras et al., 2017). The growing availability of high spatial and temporal resolution MS images has increasingly stimulated the implementation of HS-MS fusion for HS spatial resolution enhancing. Among various space missions operating MS sensors, the Copernicus Sentinel-2 mission, operated by the European Space Agency (ESA), results to be suitable for the HS-MS fusion purposes, since it includes the free-available high spatial (GSD of 10 m) and temporal (revisit time of 5 days under the same viewing conditions) resolution. Exploiting Sentinel-2 MS information is interesting from both a qualitative and operative point of view. Alicandro et al. (2022) showed an optimal agreement between PRISMA and Sentinel-2 spectral signatures, specifically representative of pits, rocks, soils, sea and sand. Similarly, Giardino et al. (2020) and Niroumand-Jadidi et al. (2020) observed strong spectral consistency between the two sensors, in the visible (VIS) and NIR region (VNIR) at TOA and BOA respectively, while analysing water bodies. Also in forest land covers, high similarity between the overall signatures of the two sensors was reported (Vangi et al., 2021).

Several pansharpening and HS–MS fusion algorithms have been developed. Vivone et al. (2021) published an exhaustive benchmark on the main pansharpening methods for multispectral images, while Yokoya et al. (2017) focused on the fusion of hyperspectral and multispectral data. Dian et al. (2021) and Sara et al. (2021) reviewed the latest advances on HS-MS fusion, while Li et al. (2022) provided a comprehensive survey focused on deep learning approaches. Vivone (2023) proposed the last survey on this topic. Specific approaches to HS-MS fusion, broadly distinguishable in matrix-factorization, Bayesan and deep learning methods, have reached superior performances compared to earlier pansharpening-derived models (Sara et al., 2021; Selva et al., 2015; Yokoya et al., 2017), especially in dealing with spectral and spatial discrepancies between HS and MS or PAN information (Dian et al., 2021; Qu et al., 2022; Simões et al., 2015; Vivone et al., 2023). Although there is growing interest toward advanced neural network architectures (e.g. convolutional neural network, generative adversarial network) due to the very promising and constantly improving results (Dian et al., 2021; He et al., 2021; Li et al., 2022; Qu et al., 2022), different issues limit their practical application, such as the training requirements (thousands of samples which are hard-to-obtain), high computational costs, limited generalization capabilities, and complex parameters setting (Dian et al., 2021; He et al., 2021; Qu et al., 2022; Vivone et al., 2023). Such limitations were pointed out by Kremezi et al. (2021). Conversely, matrix-factorization methods, especially those adopting unmixing approach to define image spectral priors, have achieved the most balanced ratio between quality of fused results, reduced reconstruction error, generalization, training-independence and efficiency of implementation (Dian et al., 2021; Lanaras et al., 2017; Sara et al., 2021; Wei et al., 2015; Yokoya et al., 2017).

In unmixing-based methods, extensively employed in HS-MS fusion framework (Brezini and Deville, 2023), the spectral information of each HS pixel is approximated as a mixture of pure spectral signatures (endmembers) in different proportions (abundance). Adopting the MS data as reference, the matching (HS-MS) spectral dictionary is then reconstructed at enhanced resolution, accounting, at pixel level, for the endmembers abundances, as well as for the relative spectral and spatial characteristics of the two sensors to improve the quality of reconstruction, described by the spectral response function (SRF) and the point spread functions (PSF) respectively (Dian et al., 2021; He et al., 2021; Lanaras et al., 2017; Simões et al., 2015; Veganzones et al., 2016; Yokoya et al., 2017). Simões et al. (2015) proposed the hyperspectral super-resolution model (HySure), an optimized unmixing-based algorithm that formulates the fusion problem as a minimization of a convex objective function in a low-dimensional subspace configuration retrieved from the low-resolution HS image. Two very attractive features of HySure are the automatic estimation of relative SRFs and PSFs included in its fusion processing, and its ambivalence in being able to be applied for pansharpening, though it was designed for HS-MS fusion. This capability made HySure widely applied in the literature (Acito et al., 2022; Brezini and Deville, 2023; Lanaras et al., 2017; Yokoya et al., 2017), with several scholars (Acito et al., 2022; Lanaras et al., 2017; Wang et al., 2021) that adopted it as a robust baseline reference algorithm for results validation.

The application of any image fusion and/or pansharpening process requires a correct geometric co-registration of the images as a pre-requisite, since even small misalignments could turn into significant errors in the image fusion outputs (Yokoya et al., 2017). Co-registration is also necessary when different sensors (with different SNR, SRF, etc.), at different spatial resolution, are fused or compared. The success of the co-registration depends on how many reliable correspondences can be found between the two images, and on the level of homogeneity of their distribution along the entire scene (Barazzetti et al., 2014). PRISMA HS images present a geolocation accuracy up to 200 m (mission requirements $\leq$ 400 m), variable between scenes and within the single scene. Alicandro et al. (2022), for example, who adopted PRISMA imagery for archaeological investigations, perceived the necessity of an improved georeferencing. Angelopoulou et al. (2023), had to enforce a manual selection of ground tie points on which a second-order polynomial model was applied to rectify the residual geometric shift to 1–2 pixels on PRISMA images. Vavassori et al. (2023) and Amieva et al. (2023) adopted an automatic non-parametric coregistration algorithm (Geoscience Extended Flow Optical Lucas-Kanade Iterative, GeoFolki) to correct PRISMA's geolocation for classification purposes. Automatic co-registration methodologies mainly differ for the image matching algorithms. Well-known are the feature-based strategies, such as the Scale Invariant Feature Transform (SIFT) (Lowe, 1999) and the Speeded Up Robust Features (SURF) (Bay et al., 2008), that rely on the detection of common and distinct object on the scenes (Bay et al., 2008; Scheffler et al., 2017), however, significantly reduced in the case of data coming from different sensors and/or with different spatial resolution (Vakalopoulou et al., 2019). The intensity-based is another class of methods that are based on the identification of corresponding grey value patterns between reference and target image (Scheffler et al., 2017). While earlier intensity-based methods suffered from sensibility to image deformations, and from high computational requirements (Long et al., 2016), recently Scheffler et al. (2017) proposed the AROSICS (Automated and Robust Open-Source Image Co-Registration Software) open-source tool, adopting an optimized phase-based correlation procedure, aiming at the sub-pixel co-registration of multi-sensor remote sensing images and able to operate also with data at different pixel resolution. Phase-based subcategory methods exploit the translation property of the Fourier transformation to measure displacements between two images in the frequency domain. Since the dominant shift is highly recognizable by a sharp peak in the cross-power spectrum, they resulted more accurate and insensitive to temporal land albedo variations than other intensity-based methods, even in poor SNR conditions (Gianinetto and Scaioni, 2008; Long et al., 2016; Scheffler et al., 2017; Skakun et al., 2017; Zitová and Flusser, 2003). The AROSICS tool is widely adopted due to its effectiveness in achieving sub-pixel accuracies, in overcoming multi-sensor and multi-resolution limits, in requiring few input parameters to set, in computational efficiency, in its user-friendly layout (Brotoisworo et al., 2022; Stumpf et al., 2018). However, as far as we know, among the few contributions that dealt with the absolute georeferencing correction of PRISMA data (Amieva et al., 2023; Vavassori et al., 2023), no experiments have implemented this cutting-edge algorithm. This study represented a useful opportunity to test it on a such geo-incorrect imagery, by adopting Sentinel-2 as geometric reference. Actually, in Cogliati et al. (2021) the application of AROSICS was limited to the detection of displacement between VNIR and SWIR bands of L1 PRISMA data.

To the extent of our current knowledge, only few studies dealt with the spatial resolution improvement of PRISMA HS images, most applying HS-PAN pansharpening methods Kremezi et al. (2021) Vivone et al. (2023), while only Acito et al. (2022) proposed a HS-MS fusion approach.

The aim of this study is therefore to propose a robust methodology capable of addressing at the same time two issues affecting PRISMA HS images: i) solving the well-known geometrical displacement of PRISMA; ii) optimally improving the spatial resolution by preserving as much as possible both spatial and spectral information. For these purposes, a HS-MS co-registration and fusion workflow was implemented, using Sentinel-2 MS data as spatial and spectral reference on different scenarios. Fusion results were also extensively compared with HS-PAN pansharpening using the panchromatic PRISMA band. Two well-know and robust algorithms were adopted to fulfil the objectives, never fully employed on PRISMA imagery: AROSICS for co-registration, and HySure for both fusion and pan-sharpening. A strength of the present study was the availability of independent airborne high-resolution HS images to be used as reference for the quantitative assessment of the fused and pan-sharpened results. Finally, guidelines are provided for adopting the optimal HS satellite data processing strategy, focused on PRISMA but scalable to other similar present and forthcoming missions, exploiting either panchromatic or Sentinel-2 data in combination with HS data.

2. Data and methods

2.1. Study area

Three study areas were selected (Fig. 1), located in the Italian territories of Grosseto (N42°82′94″, E11°06′96″), Prato (N42°87′99″, E11°08′93″) and Arborea (N39°80′15″, E8°60′44″), representing different land use spatial distributions including anthropic and semi-natural landscapes. Grosseto study area is composed by medium-small agricultural fields, interspersed by small rural urban/industrial settlements; a forest area is present in the north-west part of the scene. Prato area includes urban and industrial patterns, surrounded by agricultural fields and semi-natural areas. Arborea area is a cropland, with a complex mosaic of large and small farms.

2.2. Image datasets and pre-processing

2.2.1. PRISMA

The PRISMA HS system spans a wavelength range of 400 to 2500 nm, distributed among 239 bands with a spectral sampling interval $<$ 12 nm, and it is composed by two hyperspectral cubes: the VNIR (66 bands, 400–1000 nm) and the SWIR (173 bands, 1000–2500 nm). Adopting a push-broom image scanning mode, with a swath of 30 km (across track), covering 1000 pixels, field of view (FOV) of 2.77°, the GSD is of 30 m (ASI - Agenzia Spaziale Italiana, 2020). The PAN frame, projected on the same swath, but covering 6000 pixels with its 5 m of GSD, is appended to the HS cubes. It covers the VIS spectral range between 400 and 700 nm. The satellite revolves in a circular Sun-synchronous low-Earth orbit, with a repeat cycle of around 29 days and with a $<$ 7 days potential revisit pass (off-nadir), for on-demand specific requested target (Giardino et al., 2020; Pepe et al., 2020).

In this work, for all the study areas, PRISMA standard Level-2D products were used, containing bottom-of-atmosphere (BOA) reflectance derived by a MODTRAN-based atmospheric correction of the at-sensor radiance (processor v.02.05). The product is *ortho*-projected and geocoded in UTM projection (EPSG: 32632), without use of external ground control points (GCPs). Four cloud-free images were acquired through on-demand request during PRISCAV survey campaign (Table 1): Grosseto 31st July and 1st August 2020; Prato 27th June 2020; Arborea 30th May 2022.

The preliminary band selection consisted of three steps: a) automatic elimination of "zero bands", i.e. defective bands flagged as zero in metadata and/or bands with zero-valued pixels $>$ 90 % out of the total; b) exclusion of spectral bands corresponding to water vapor absorption windows between 1350–1470 nm, 1800–1950 nm, and, as stated by Alicandro et al. (2022), at around 920, 1120 and 2020 nm; c) exclusion of bands poorly correlated to neighbouring ones (e.g. "salt-and-pepper", "Gaussian like" noise), including the first 3 bands (406.9——423.8 nm) of VNIR and the last 23 bands of SWIR (2342.8——2477.1 nm) were also filtered out. The final HS spectral cube, consisting of 167 bands, did not vary among the four datasets.

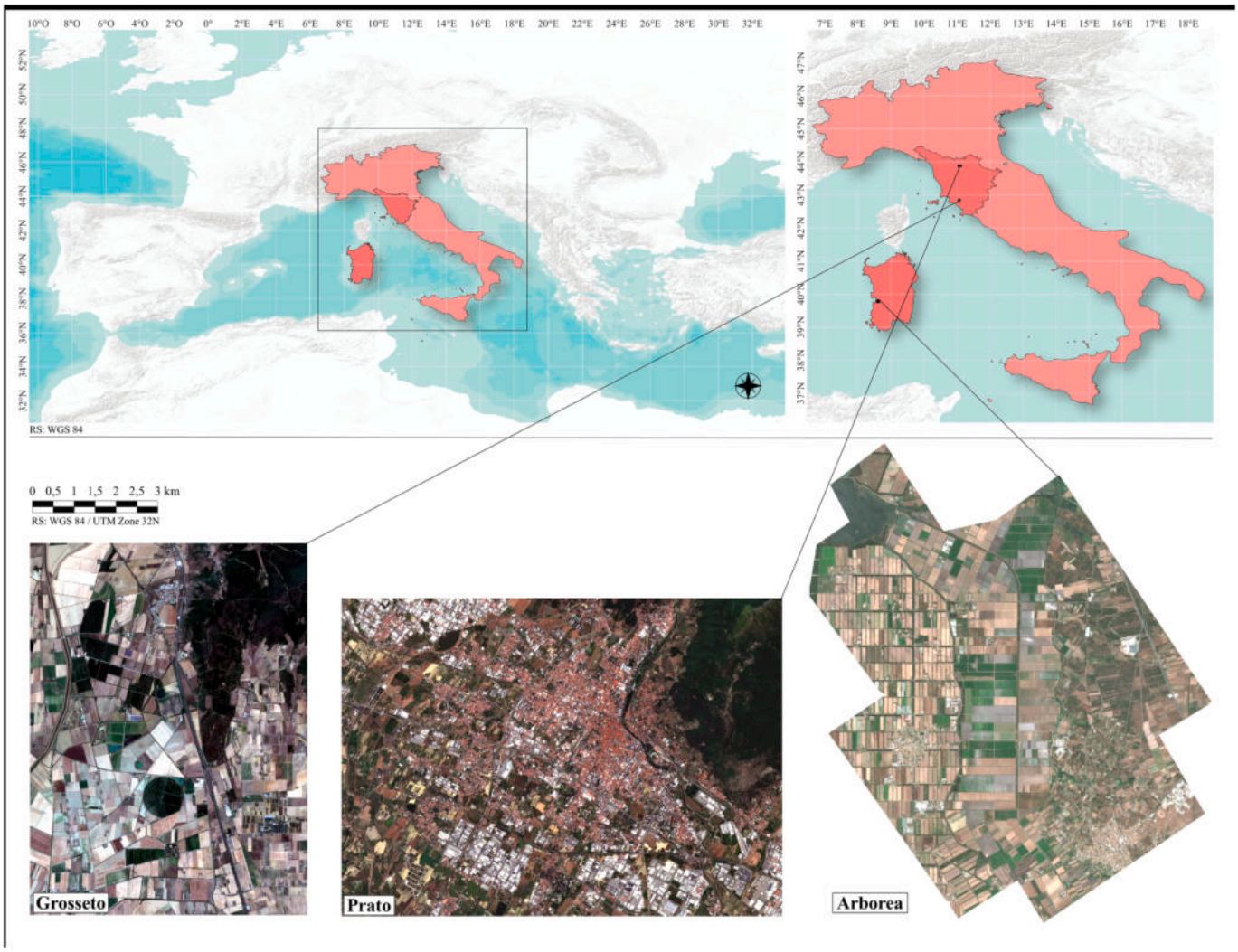

Fig. 1. Continental and national location of the study areas (on the top). On the bottom, the true color overviews of Grosseto (left), Prato (middle) and Arborea (right) study areas.

A subset of the image was clipped for each study area (Fig. 1), matching the scene captured by an airborne HS survey (Section 2.2.3), and used as input scenes in HS-MS fusion process (Section 2.3.2); the entire PRISMA image was instead involved during co-registration process (Section 2.3.1).

2.2.2. Sentinel-2

Sentinel-2 satellites are equipped with a MS sensor – namely Multi-Spectral Instrument (MSI) – performing spectral observations between 440 nm and 2200 nm, distributed in 13 bands at 12-bit radiometric resolution, at native GSD of 10 m (VIS and NIR), 20 m (NIR and SWIR) or 60 m (auxiliary water content and cirrus bands), providing a revisit time of 5 days at mid-latitudes. Sentinel-2 Level-1C products geolocation accuracy is reported to be within 8 m (Sentinel Online, 2021). A series of Sentinel-2 Level-2A (BOA, geocoded in UTM projection data – EPSG: 32632) images covering the same study areas and as close as possible to acquisition dates of PRISMA images were retrieved (Table 1). One scene for Grosseto study area (1st August 2020, same day as the second PRISMA image), one scene for Prato (27th June 2020, same day as PRISMA), and one scene for Arborea (31st May 2022, 2 days before PRISMA) were downloaded.

The pre-processing consisted of a pixel upsampling to 10 m GSD of those bands whose native GSD was 20 m, using the red band (B4) as pixel spacing reference and the nearest neighbour interpolation as resampling method. This intra-equalization of bands' GSD was necessary in anticipation of the HS-MS fusion. The open-source SNAP v.9

Table 1
Employed data schematization. (N42°87′99″, E11°08′93″) and Arborea (N39°80′15″, E8°60′44″).

Study Area	PRISMA Date	Roll angle	Sentinel-2 Date	Airborne Date	Payload
Grosseto	31st July 2020	−12.7°	1st August 2020	31st July 2020	CASI/SASI
(N42°82′94″, E11°06′96′)	1st August 2020	+17.0°		1st August 2020	CASI/SASI
Prato	27th June 2020	+8.3°	27th June 2020	22nd June 2020	HySpex (VNIR/SWIR)
(N42°87′99″, E11°08′93″)					
Arborea	30th May 2022	+13.6°	31st May 2022	30th May 2022	CASI/SASI
(N39°80′15″, E8°60′44″)					

software (ESA SNAP Cookbook, 2024), implemented via the SNAP-Python API interface (snappy), was used to perform the pre-processing. The final multispectral bands involved in subsequent analyses were Blue (B2), Green (B3), Red (B4), Red-Edge01 (B5), Red-Edge02 (B6), Red-Edge03 (B7), NIR (B8), SWIR01 (B11), SWIR02 (B12).

The entire Sentinel-2 images were employed to co-register the entire PRISMA HS imagery. Successively, the first were clipped according to PRISMA HS subset (Section 2.2.1.) to be involved in the HS-MS fusion step.

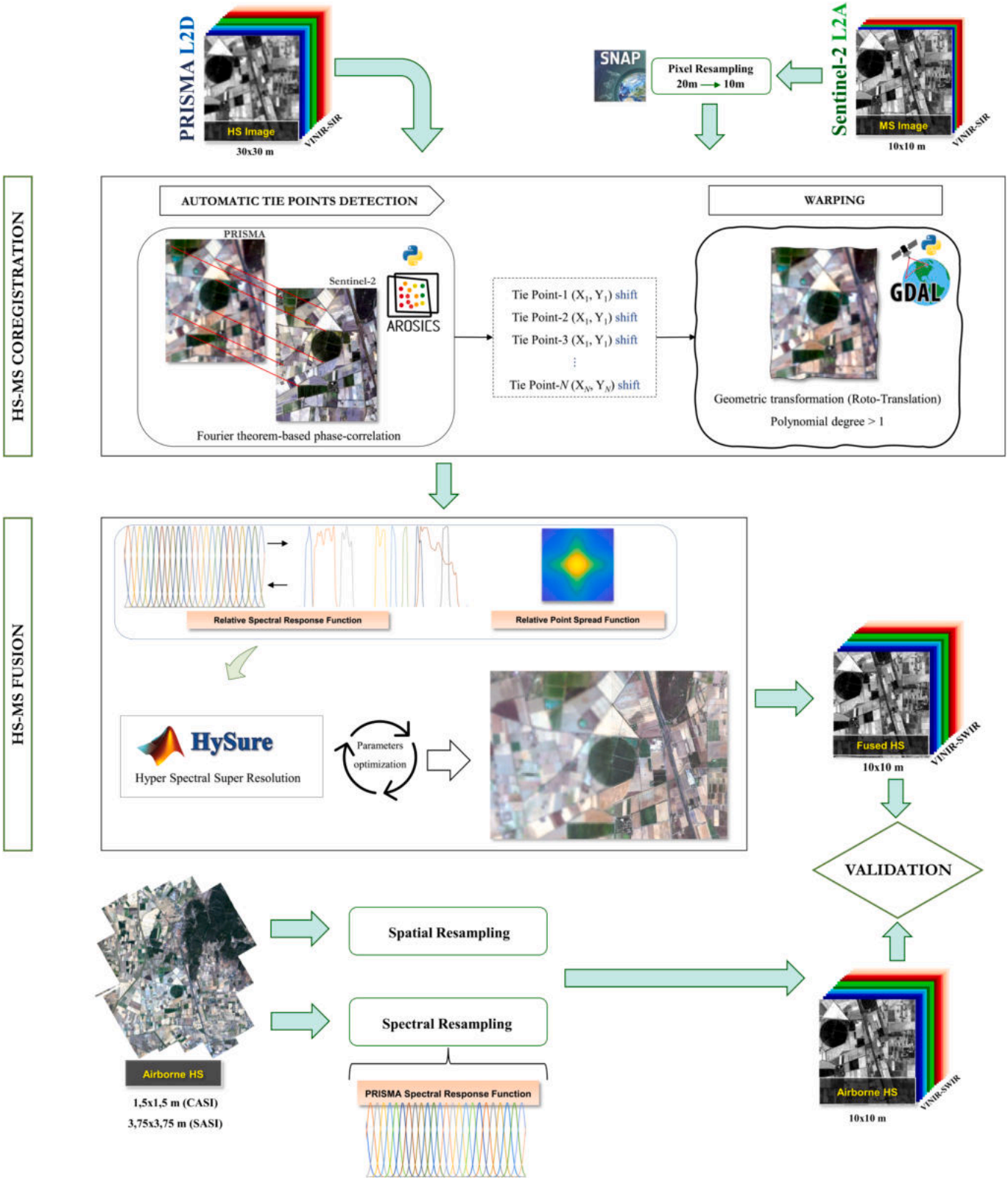

Fig. 2. Flowchart schematizing the HS-MS fusion processes that characterized the present study.

2.2.3. Airborne data: CASI/SASI and HySpex VNIR/SWIR

At Grosseto and Arborea sites, airborne HS measurements were made simultaneously with PRISMA overpasses (in clear-sky conditions) within the PRISCAV project operating a CASI/SASI (compact VNIR/SWIR airborne spectrographic imager) payload; at Prato site, airborne HS measurements were made 4 days before PRISMA overpass operating a HySpex sensors payload (Table 1). CASI/SASI data were made available within the PRISCAV project, while HySpex data are freely available from Tuscany regional administration.

The CASI/SASI (Itres Reasearch ltd., Canada) consist of two push-broom sensors (jointly mounted on gyro-stabilisation platform): the CASI-1500, covering the VNIR spectral range within 380 and 1050 nm, distributed over 96 bands, with a spectral sampling interval of 7.2 nm; the SASI-600, covering the SWIR between 950 nm and 2450 nm by 100 bands, with a sampling interval of 15 nm. The spectral distance between central wavelengths of PRISMA HS and CASI/SASI sensors never exceeded 3 nm (CASI) and 7 nm (SASI) across the entire spectral range. The initial GSD of returned image strips was 1.5 m for CASI, and 3.75 m for SASI (Grosseto). Although for Arborea the SASI dataset was acquired, the sensor incurred in hardware technical problems during the flight that hampered the dataset.

The HySpex sensor (Norsk Elektro Optikk, Norway) incorporates two separate push-broom HS scanners, the VNIR-1800 (400–1000 nm) and the SWIR-384 (960–2500 nm). Arranging a spectral sampling interval of 3.3 nm for VNIR and 5.5 nm for SWIR, the resulting bands were 186 and 288 respectively. The spectral distance with PRISMA HS central wavelengths was $\leq \pm$ 2 nm. The GSD was 1 m for VNIR and 3 m for SWIR.

The HS images deriving from both CASI/SASI and HySpex sensors were radiometrically corrected, calibrated and *ortho*-projected. The atmospheric correction was carried out, separately for VNIR and SWIR, employing the atmospheric radiative transfer model MODTRAN-5 implemented into the ATCOR-4 software (ReSe Applications LLC, Langeggweg 3, CH-9500 Wil SG, Switzerland). The ground reflectance and radiance, collected by FieldSpec 3 instrument (Malvern Panalytical Ltd, Malvern, UK) (Grosseto and Prato) and Spectral Evolution RS5400 (Haverhill, Massachusetts, USA) (Arborea) in test areas during overflight, were assumed as reference during the calibration process. Subsequently, the image strips were mosaicked, resampled to 5 m, 10 m, and 30 m pixel spacing applying a bilinear interpolation, and the respective VNIR and SWIR spectral cubes were stacked. During this process, carried out using GDAL library (GDAL, 2024), the pixels matrices were aligned to those of co-registered PRISMA PAN, Sentinel-2 and co-registered PRISMA HS respectively. The resulting datasets were spectral resampled to the PRISMA SRF using the Spectral Resampling tool implemented in the ENVI 5.6 software (NV5 Geospatial, Broomfield, Colorado, USA), after that the noisy bands had been filtered out as already done for PRISMA HS (Section 2.2.1). The Spectral Resampling tool automatically builds the SRF on a Gaussian model employing the full width at half maximum (FWHM) as spacing values.

To overcome different reflectance scaling factors between images, all the spaceborne and airborne images were rescaled to floating point digits at 32 bits [0, 1].

2.3. Processing workflow

The proposed workflow consisted of three main processing steps, summarized in Fig. 2. Most of the procedures were carried out implementing open-source and free-available software, libraries and/or codes (Python libraries, QGIS, SNAP). Excluding the validation process, in which the pre-processing steps of airborne data required commercial software, the HS-MS fusion model was the only operative phase of the workflow to have been carried out using a non-open-source environment (MATLAB).

Table 3
HySure parameters and respective set of values combinations tested during tuning.

HySure parameter	Description	Values tested
λ_m λ_ϕ	regularization parameters (control the optimization terms)	1, 20, 50, 08 0.001, 0.005, 0.01, 0.05 0.1
p	subspace dimensionality (number of endmembers) of HS image that was expected to be retrieved from VCA	2, 10, 25, 50
λ_R	Regularization parameter for relative SRF auto-estimation	5, 10, 50
λ_B	Regularization parameter for relative PSF auto-estimation	5, 10, 50
X/Y windows size	X/Y dimension (pixels at highest resolution) of convolution kernel size (2D cyclic convolution) that supports the auto-estimation of PSF	5, 10, 15

2.3.1. Image co-registration

The AROSICS algorithm (Scheffler et al., 2017) applies an improved phase-correlation approach (Foroosh et al., 2002), employing discrete Fourier transformation domain (Fastest Fourier Transform in the West, FFTW) (Bracewell and Kahn, 1966; Frigo and Johnson, 2005, 1997) to derive pixel geometrical displacement among a pre-constructed grid of tie points. The detailed description of the algorithm is available in Scheffler et al. (2017). In this study, the *local co-registration* algorithm was employed instead of *global co-registration*. The algorithm presented some intuitive parameters that were easily set during the main steps of its chain process (Table 2). In detail, it applies the phase-correlation algorithm toward a moving window across a regular pre-set grid of tie points, so as the magnitude of the shift for each tie point is estimated locally.

As a prerequisite for the application of phase correlation, the spatial resolution of the two images (reference-target) is temporarily equalised by an automatic image down-sampling, a highlight overpassing the different spatial resolutions issue. A *reliability* score [0–100 %] is first calculated for each tie points to filter them by applying the formulas (3), (4), (5) and (6) in Scheffler et al. (2017), which aim to analyse the three-dimensional shape of the cross-power spectrum and to quantify peak sharpness. The final thresholding filtering was performed by excluding all the points presenting *reliability* score $<$ 75 %, although Scheffler et al. (2017) declared that the points can be maintained until the 30 % *reliability* threshold.

The local X/Y shift values detected for each tie point were finally adopted for the construction of a second-order polynomial geometric transformation function, to warp the target image and then correct the misregistration with the respective reference image. In the original AROSICS tool, only the first-order polynomial function is available for

Table 2
AROSICS parameters set for the estimation of X/Y shift.

PARAMETER	VALUE	DECRIPTION
Moving window size	15x15 pixels	X/Y size of moving window; number of pixels adopting the resolution of target image
Grid resolution	30x30 pixels	X/Y distance of tie points within the generated dense grid; number of pixels adopting the resolution of target image
Resampling algorithm	nearest neighbour	the resampling algorithm used during the automatic temporary equalization of spatial resolution between target and reference images
Max iterations	25	maximum number of iterations during matching process
Maximum shift	30 pixels	maximum tolerated X/Y shift threshold beyond which the point is considered unrealistic and thus the respective tie point is rejected.

shift correction. This did not result suitable enough to fit the actual geometrical displacement found in PRISMA. In our application, the source code was therefore integrated with a second-order polynomial, through GDAL library. The nearest neighbour resampling method was used to minimize the eventual manipulation of the original pixel values.

To improve the correspondences detection, by minimizing the residual measurement errors (Scaioni et al., 2018), the algorithm was iterated for each reference-target (Sentinel-2 – PRISMA) band pairs that present the closest central wavelength (e.g. B2-B12, B3-B21), for a total of 9 matches (the number of employed Sentinel-2 bands). For each match, the point grid was reinstituted reporting the specific X/Y shift estimated for that bands pair. The final grid, reporting the X/Y shift

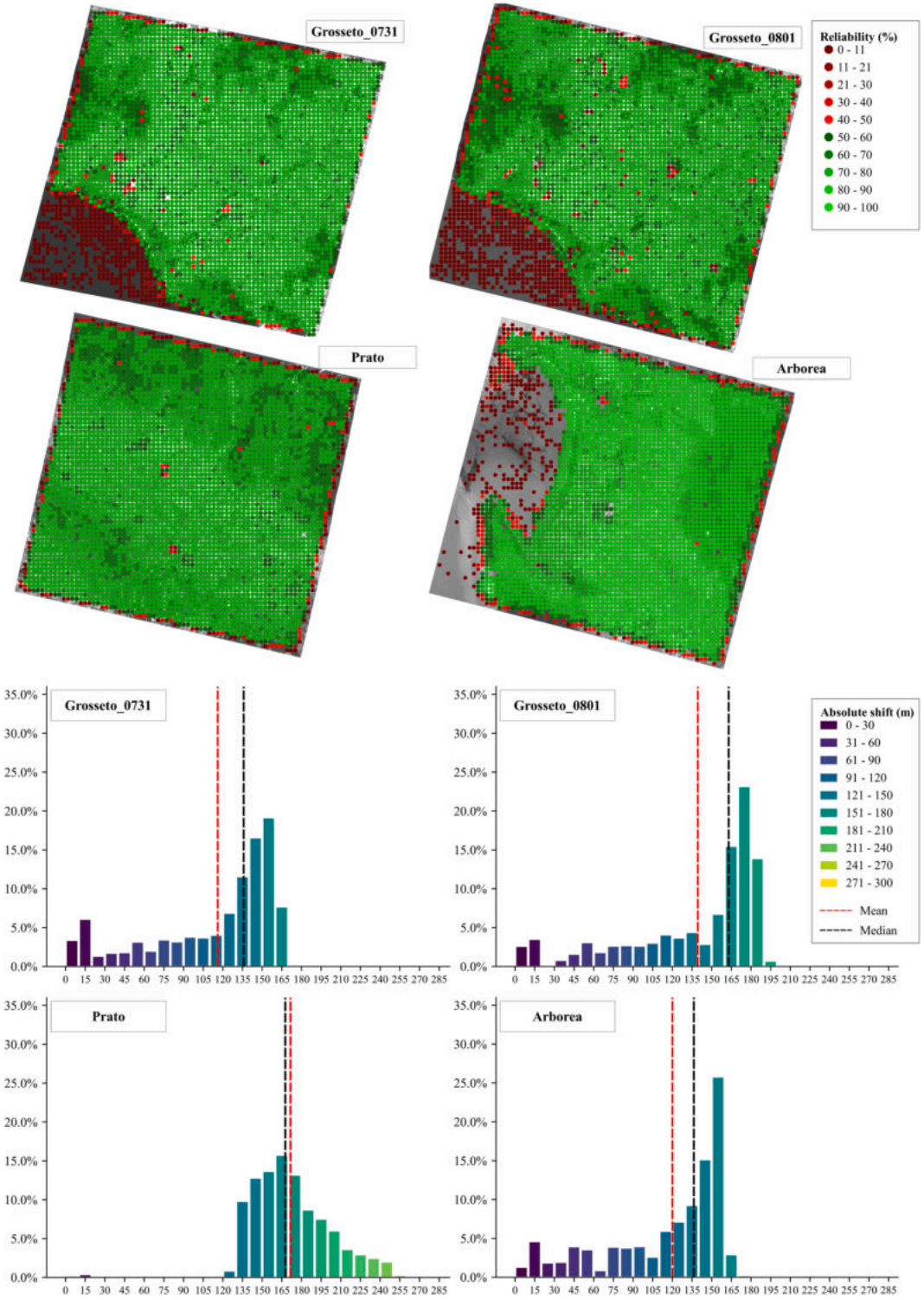

Fig. 3. Spatial distribution of tie points grid on the entire PRISMA HS image for the four scenes Grosseto_0731, Grosseto_0801, Prato and Arborea, as resulted by the co-registration algorithm, vested by a color palette indicative of the *reliability* score (on the top). On the bottom, the respective histogram plot reporting the frequency of the absolute shifting magnitude (in meters) among points, with the mean (red dashed line) and median (black dashed line) values pointed out. (For interpretation of the references to color in this figure legend, the reader is referred to the web version of this article.)

values employed in successive processes, was retrieved by applying a composite process, in which, for each tie point, the X/Y shift of the one that reached higher *reliability* in the respective 9 reference-target matches was chosen to be included in the final grid.

After having quantified and corrected the surface displacement of the entire PRISMA HS/PAN images, all the following analysis were conducted on a subset of the whole PRISMA scene to target the central part of the scene.

2.3.2. HS-MS fusion and HS-PAN pansharpening

The state-of-the-art HySure (Simões et al., 2015, 2014) was implemented via MATLAB to both fuse PRISMA HS and Sentinel-2 MS images and apply pan-sharpening between HS and PAN.

The algorithm addresses the fusion problem as a minimization of a convex objective function in a subspace configuration retrieved from the low-resolution HS image. Specifically, the model integrates the well-known VCA algorithm to estimate the subspace dimension, a rapid technique that reduces the processing time in endmember extraction (Brezini and Deville, 2023), acting as a matrix linear unmixing problem. The ill-posed nature of the reduce-dimensionality problem makes it necessary the implementation of an edge-preserve regularization process, also integrated into HySure in the form of VTV (Bresson and Chan, 2008), accounting for both spatial and spectral sensor specifics (Simões et al., 2015). Finally, the convex optimization is solved by the Split Augmented Lagrangian Shrinkage Algorithm (SALSA), which applies the Alternating Direction Method of Multipliers (ADMM) optimization method (for an exhaustive explanation of the algorithm, please refer to (Simões et al., 2015).

Matching spatial and spectral responses of the two sensors is needed to maintain a physical significance of the fusion process (Brezini and Deville, 2023; Inamdar et al., 2020; Lanaras et al., 2017; Otazu et al., 2005). The HySure way to calculate the relative SRF and PSF of the two sensors is data-driven from the images, approaching it as another convex quadratic optimization problem (Simões et al., 2015).

The HySure model depends on several parameters (Table 3). The best combination of model parameter values was set by careful tuning, adopting the combination that resulted in the best accuracy assessed among the various tested ones, thus adapted to each specific dataset and separately for HS-MS fusion and HS-PAN pan-sharpening. The evaluation of tuning results was carried out both visually and analytically, by applying the accuracy assessment procedure (validation data and accuracy metrics) as implemented in Section 2.3.3. The values setting was however initialized in accordance with the suggestions provided by the original authors (Simões et al., 2015) and successive implementation by other scholars (e.g. Yokoya et al., 2017).

Performing the ADMM approach for optimization increases the computational cost, counterbalanced by setting an appropriate number of iterations (Acito et al., 2022). The number of iterations for ADMM was set to 200 (default) as suggested by (Simões et al., 2015).

2.3.3. Accuracy assessment

Quantitative and qualitative evaluation of the fused images was performed by measuring their spectral and spatial consistence with respect both the original HS images and the high-spatial HS reference dataset, using different metrics. A first assessment relied on the visual comparison between spectral signatures of fused/pansharpened image (output) and the high-resolution (resampled at 10 m or 5 m respectively) airborne HS data (reference). For a more exhaustive comparison, the signatures of the original PRISMA image and Sentinel-2 were also integrated into the same comparison. Spectral signatures were retrieved over a series of region of interests (ROIs). ROIs had the size of PRISMA's original GSD (30 m) and, therefore, each ROI is contained in at least 1 PRISMA pixel, 9 fused/Sentinel-2 pixels and 36 pan-sharpened pixels. These ROIs were carefully chosen by visual inspection to be purely representative (at all resolutions) of three macro land user/cover (LUC) on the scene (green vegetation, bare soil, urban), while a small part which laid at the border between two adjacent LUCs (e.g. soil-green vegetation) is used to detect the presence of edge-artefacts. In total, 40 ROIs for each study area (10 per LUC) were retrieved, distributed around the whole scenes to be as representative as possible of the land use and spatial heterogeneity distribution.

To perform a robust and comprehensive accuracy assessment of both the HS-MS fusion and HS-PAN pan-sharpening outputs, several state-of-the-art validation metrics were computed on a pixel basis. The root means square error (RMSE) between the fused/pansharpened image, and the reference truth was calculated for each pixel (RMSEP), and for each band according to:

$$RMSE_P = \sqrt{\frac{1}{nb}\sum_{ib=1}^{nb}(p_{ib} - \hat{p}_{ib})^2} \tag{1}$$

$$RMSE_b = \sqrt{\frac{1}{np}\sum_{xy=1}^{np}\left(p_{xy} - \hat{p}_{xy}\right)^2} \tag{2}$$

where the symbol ˆ differentiates the reference truth image, p_{ib} indicates the pixel i for a specific band b; nb is the number of bands; p_{xy} indicates the pixel in the xy position on the specific analysed image band; np is the number of pixels in the specific analysed image band.

The Spectral Angle Mapper (SAM) (Yuhas, Goetz, and Boardman 1992) was used to calculate the per-pixel angle between each i^{th} pixel spectrum (x) of fused/pansharpened image and the respective pixel spectrum of the reference truth image ($\hat{x}$) (SAM_p). The SAM, expressed in in radians [0, π], measures the spectral similarity of the compared pixels, by comparing the shape of their spectra. The more the SAM value tends towards 0, the lower the spectral distortion, indicating higher spectral affinity between the compared spectra. The average over all pixels was also computed as quality summary indicator of the entire fused/pansharpened output.

$$SAM_p = arcos\left(\frac{\sum_{i=1}^{nb}(x_i \bullet \hat{x}_i)}{\|x_i\|_2\|\hat{x}_i\|_2}\right) \tag{3}$$

The peak signal-to-noise ratio (PSNR) stands for the spatial reconstruction quality of the fused/pansharpened product. For each band $PSNR_b$ is computed while the summary quality measure of the entire output is retrieved by averaging the PSNR value over all bands. It is expressed in decibel (dB) and directly proportional to the similarity between the compared images, with higher values corresponding to higher spatial reconstruction quality.

$$PSNR_b = 10 \bullet \log_{10}\left(\frac{max(x_i)^2}{\|x_i - \hat{x}_i\|_2^2/P}\right) \tag{4}$$

where P represents the number of pixels in a band; $\max(x_i)^2$ is the maximum pixel value in the specific band.

Finally, the universal image quality index (UIQI) was employed as final evaluator of the spectral correlation between the two images. The UIQI value ranges between −1 (highest spectral distortion) and 1 (lowest spectral distortion). The $UIQI_b$ was computed for each band, while the average value among bands was retrieved as summary quality metric of the entire output.

$$UIQI_b = \frac{4 \bullet \delta_{x\hat{x}} \bullet \mu_x \bullet \mu_{\hat{x}}}{(\sigma_x^2 + \sigma_{\hat{x}}^2) \bullet (\mu_x^2 + \mu_{\hat{x}}^2)} \tag{6}$$

where $\delta_{\hat{x}x}$ is the covariance between reference and fused/pansharpened, while σ^2 and μ denote their variance and mean respectively.

Signatures comparison and validation metrics calculation were performed via Python libraries.

3. Results

3.1. Geometrical displacement of PRISMA

The semi-automatic process for image co-registration, made with AROSICS algorithm, returned several information about the geolocation error affecting PRISMA images. The by-product of this process, the tie point grid, which consisted of around 3550 (Grosseto, both dates), 3650 (Prato) and 3910 (Arborea) correspondences respectively, provided i) the spatial distribution of the X/Y shift of each point, ii) the respective direction shift vector, iii) the magnitude of the X/Y shift of each point, and iv) a *reliability* score computed to filter low-standard correspondences (*reliability* < 75 %). Only the latter two information have been reported here (Fig. 3), meanwhile the first two ones are consultable in the supplementary material attached to this manuscript.

Most of the tie points had high values of *reliability* in all the study areas. The unreliable points observable in the figures (tending towards red) are for illustrative purposes only. These points were in fact excluded during the filtering procedure before applying the warping process.

The magnitude of the spatial shift is quite homogeneous among the two images focused on Grosseto and Arborea. A slight difference is observable in Prato compared to the other areas, especially for the frequency distribution among points. Highest shifts were found in Prato (mean 170 m and median 172 m), while Grosseto_0731 reached lowest average displacement, whit a mean shift of 118 m. In both Grosseto areas and Arborea, values that regularly hovered around zero are observable.

3.2. Image fusion and pansharpening

Table 4 shows the resulting averaged (and respective standard deviation) scoring of RMSE, SAM, PSNR and UIQI overall accuracy metrics, obtained by comparing the HySure outputs (fused or pansharpened) with the respective airborne images reference. For a more consistent assessment, the accuracy metrics calculated for each band (RMSEb, UIQIb and PSNRb) are plotted in Fig. 4, while the spatial distribution of the per-pixel accuracy is represented by the RMSEp and the SAMp maps in Fig. 5, indicating the magnitude and the spectra angle of the error at each pixel spectrum (Yokoya et al., 2017). The relative cold-warm color palette adopted for the two maps describes the level of spectral similarity of each pixel: the warmer the color (yellow), the worse the spectral quality; the colder the color (dark blue, RMSEp; dark purple, SAMp), the greater the spectral similarity. It is important to remind that for Arborea study area, only the VNIR part of the spectrum was analyzed, due to the unavailability of the airborne SASI SWIR reference image.

The overall spectral similarity is very high for all configurations, with a better performance of the fusion process output as compared to the pansharpened. The worst performance in terms of RMSE, SAM and UIQI are found in the Prato area. Nevertheless, even in the worst case, the absolute error values are relatively small (worse average RMSE = 0.071, worse average SAM = 0.187 rad and worse average UIQI = 0.594). The spectral dissimilarity is confirmed by the average values expressed as a function of the spectral bands (Fig. 4), for which the pansharpened Prato outputs reached more critical UIQIb values, corresponding to a substantial loss of nearly 0.3 with respect to the other scenes and to the fusion output of the same scene. Albeit with different intensity, this gap between accuracy metrics values of fusion and pansharpening outputs is observable in all the scenes.

Contrarily, the spatial quality metrics, empirically described by the higher PSNR values, indicates the Prato fused image as better reconstructed (25.949 dB). Both Grosseto scenes showed similar results in terms of overall and per-band accuracy, and of difference performance between the two adopted methodologies (fusion and pansharpening). This latter aspect becomes evident observing the gradient color contrast in the RMSEp and SAMp maps in Fig. 5. The pansharpened images present a slightly lower spectral quality reconstruction. As expected, higher values of RMSEp and SAMp are equally concentrated at the edges of geometrical objects/shapes on the earth's surface (e.g. edges of buildings, boundaries between one agricultural field and another, road edges, etc.). Noticeable is the greater sensitivity of the SAM index to water bodies (river in Prato and lakes in Grosseto), with high values not equally observable in RMSEp map.

The fused/pansharpened (orange line) and the original PRISMA (dashed black line) signatures, retrieved from the 40 representative ROIs, are significantly correlated along the entire spectrum in all the comparisons (slight divergences are observable only on urban surfaces). On the other hand, discrepancies are observable between PRISMA (both fused and pansharpened) and reference airborne images: in the first bands of SWIR (930 and 1300 nm), the discrepancies are common in all the scenarios, thus refuting what was observed in Fig. 4; the divergency between 730 and 920 nm observable only in Arborea and Grosseto (0731); and that one between 1500 and 1750 nm present in Grosseto 0731. These discrepancies, however, were not affected by the fusion and/or pansharpening process, as they were already observable with original PRISMA images. In general, the spectral signatures retrieved from Prato showed the best cross-sensor fit on all the analysed land covers, differently to what was observed in Table 4.

The visual interpretation of results is still a very strong error indicator (Vaiopoulos and Karantzalos, 2016; Wang et al., 2021), and supported the accuracy assessment. In particular, the careful band-by-band inspection of all the tested outputs made it possible to see how, in most spectral bands, the HS-MS fusion process outperformed HS-PAN pansharpening in terms of spatial information retaining. The latter, in fact, resulted affected by strong blurred artefacts in some image bands. This was found mainly in Prato and Arborea sites (Fig. 14), where the heterogeneity of the urban or intensively agricultural landscapes mosaicking is more apparent. In Prato, in particular, the blurred artefacts were noticeably present in correspondence to urban or natural green areas. However, the three true color images observable on the top of Figs. 6-13, showing, in detail, a representative region of the respective scene, highlight that both fusion and pansharpening processes performed optimally in the VIS region (similar vivid color tonality), where the spectral information obtained from MS and PAN was complete in both cases.

Table 4
Accuracy metrics values (mean and standard deviation) computed, for each study area, by comparing the PRISMA fused and pansharpened HySure outputs with the respective airborne reference HS images. The most suitable parameters values, founded for each situation, are also reported.

		RMSEp		SAM		PSNR		UIQI	
		μ	±σ	μ	±σ	μ	±σ	μ	±σ
Grosseto_0731	Fused R10 B10 p50 phi-0.005 λ_m1 10 *m*	0.039	0.014	0.095	0.035	24.983	3.309	0.932	0.025
	Pansharpened R10 B10 p50 λ_ϕ0.01 λ_m20 W10m	0.045	0.020	0.110	0.055	21.898	1.687	0.860	0.072
Grosseto_0801	Fused R10 B10 p50 phi-0.02 λm20 10 *m*	0.036	0.018	0.106	0.099	23.807	3.284	0.885	0.065
	Pansharpened R10 B10 p25 λ_ϕ0.005 λ_m1 W10m	0.042	0.022	0.123	0.106	22.566	2.096	0.838	0.073
Prato	Fused R10 B10 p50 λ_ϕ0.01 λ_m1 W10m	0.050	0.034	0.140	0.087	25.949	2.459	0.778	0.067
	Pansharpened R10 B10 p10 λ_ϕ0.001 λ_m1 W15m	0.071	0.048	0.187	0.127	24.031	2.365	0.594	0.122
Arborea	Fused R10 B55 p10 λ_ϕ0.02 λ_m1 W10m	0.018	0.022	0.105	0.099	25.114	1.742	0.911	0.049
	Pansharpened R10 B10 p10 λ_ϕ0.01 λ_m20 W10m	0.025	0.028	0.134	0.108	24.983	4.773	0.858	0.078

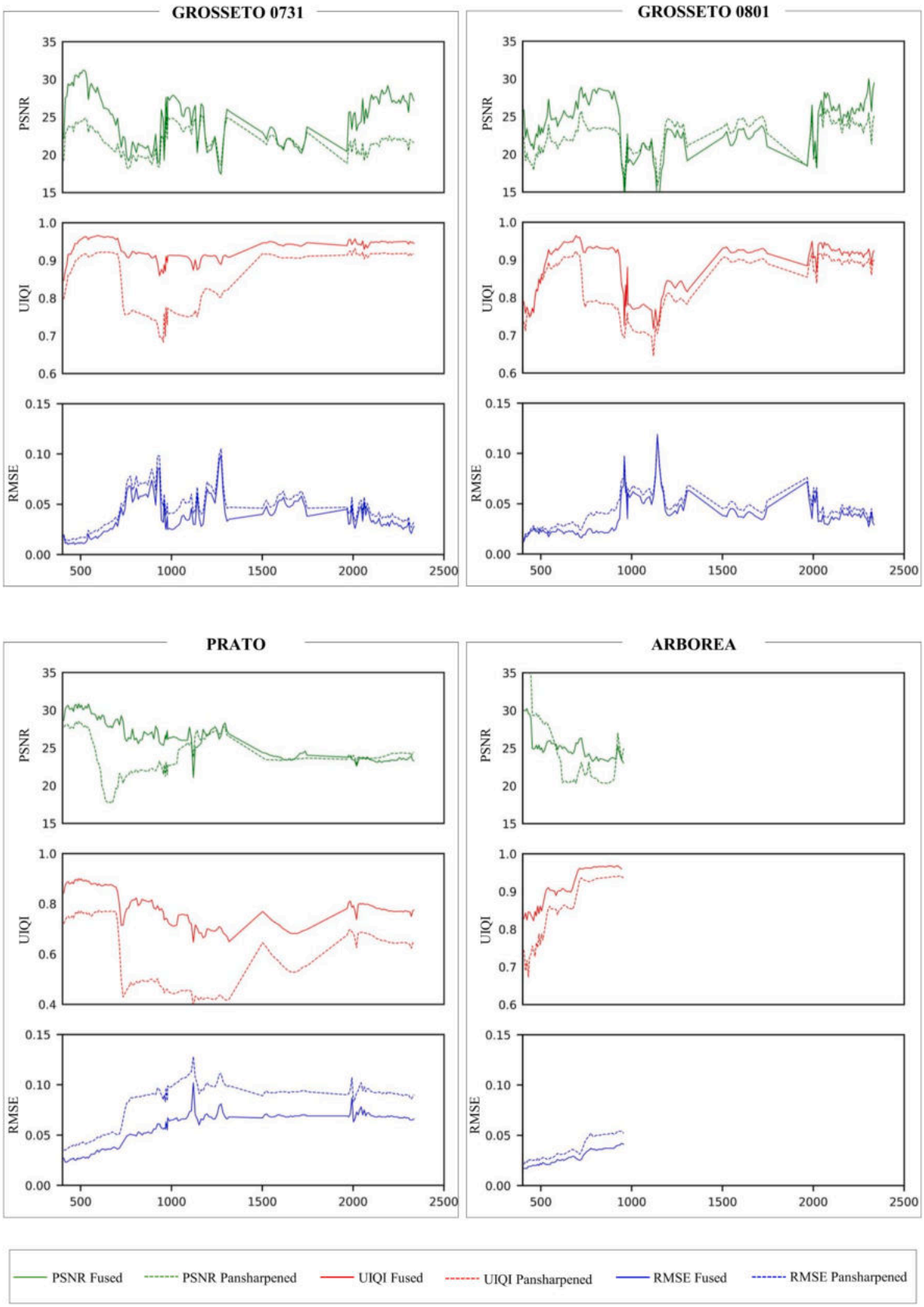

Fig. 4. The plots report the per-band accuracy metrics (RMSEb, UIQIb and PSNRb) curves, as functions of the wavelengths of the spectral bands, computed for each study area, by comparing the PRISMA fused and pansharpened HySure outputs with the respective airborne reference HS images.

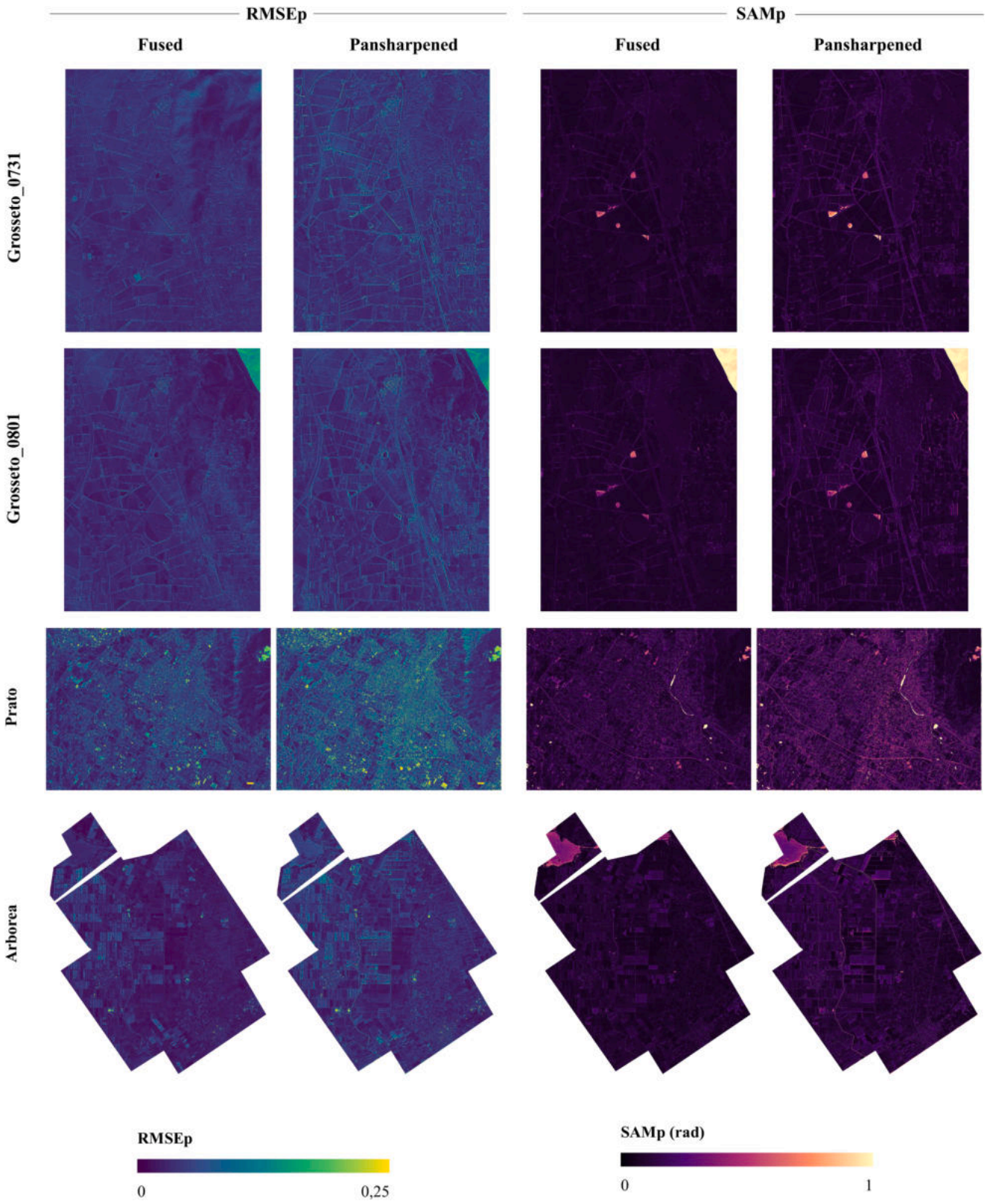

Fig. 5. Spatial distribution of per-pixel RMSE and per-pixel SAM, computed for each study area by comparing the PRISMA fused and pansharpened HySure outputs with the respective airborne reference HS images. The resulted accuracy maps generated from the HS-MS fused and the HS-PAN pansharpened outputs are placed side by side for an immediate visual comparison.

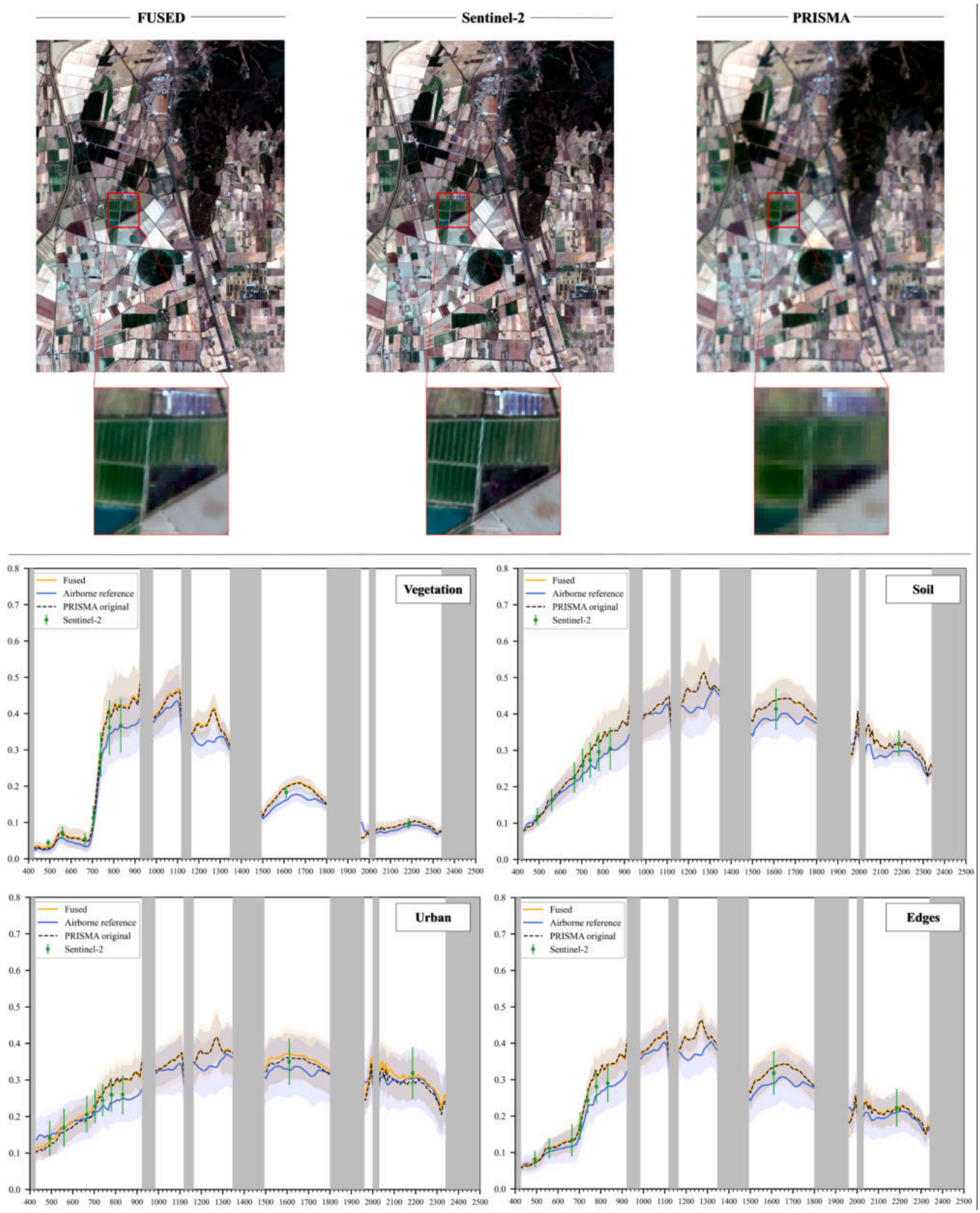

Fig. 6. Grosseto 0731 study area. On the top row: true color PRISMA fused image, as returned by HySure HS-MS fusing process (left); Sentinel-2 image (middle); original PRISMA HS image (right). On the bottom, the spectral signatures retrieved from the PRISMA fused and original, airborne reference and Sentinel-2 images are plotted, representing four representative land cover classes (vegetation, top-left; bare soil, top-right; urban, bottom-left; edges, bottom-right).

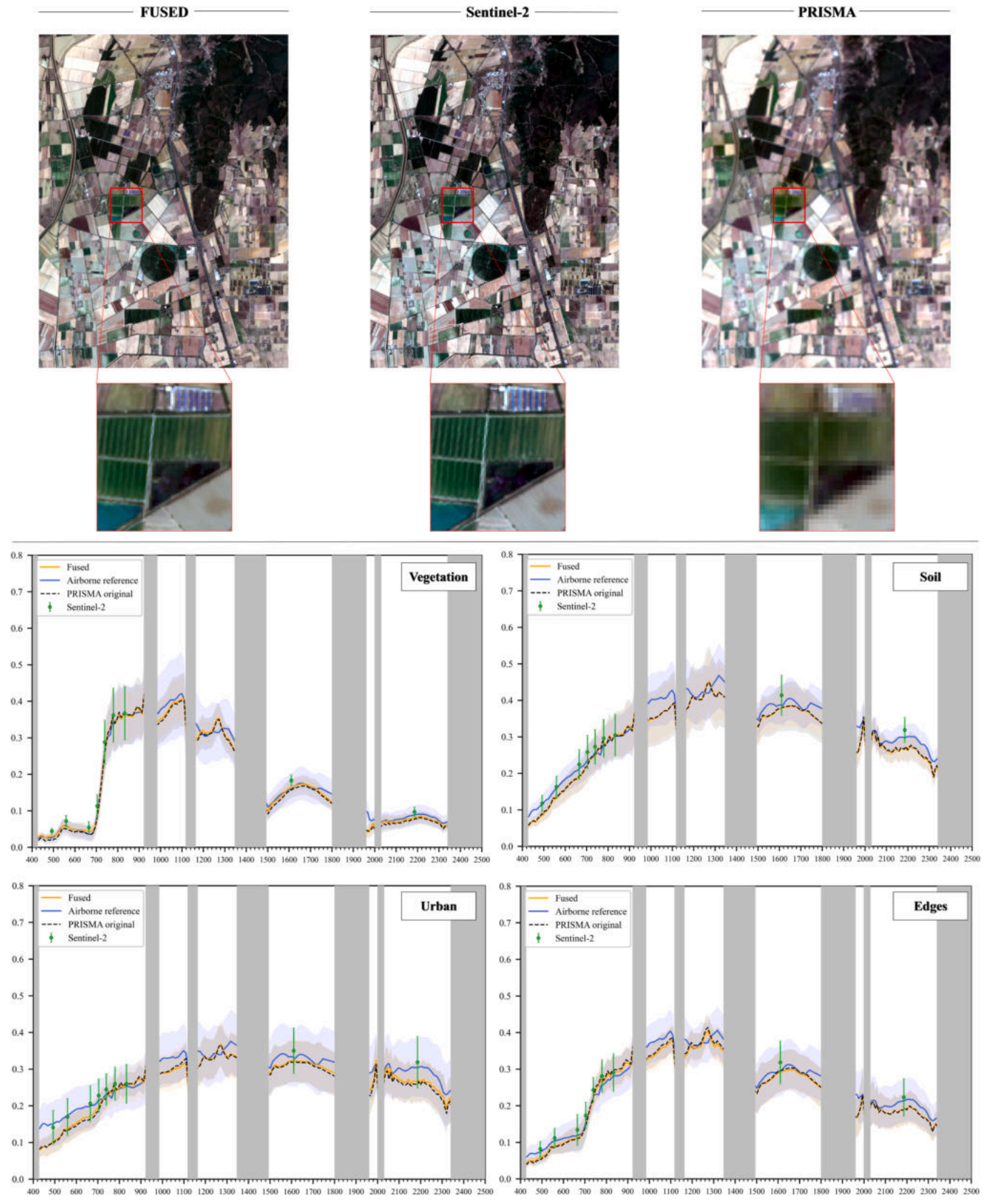

Fig. 7. Grosseto 0801 study area. On the top row: true color PRISMA fused image, as returned by HySure HS-MS fusing process (left); Sentinel-2 image (middle); original PRISMA HS image (right). On the bottom, the spectral signatures retrieved from the PRISMA fused and original, airborne reference and Sentinel-2 images are plotted, representing four representative land cover classes (vegetation, top-left; bare soil, top-right; urban, bottom-left; edges, bottom-right).

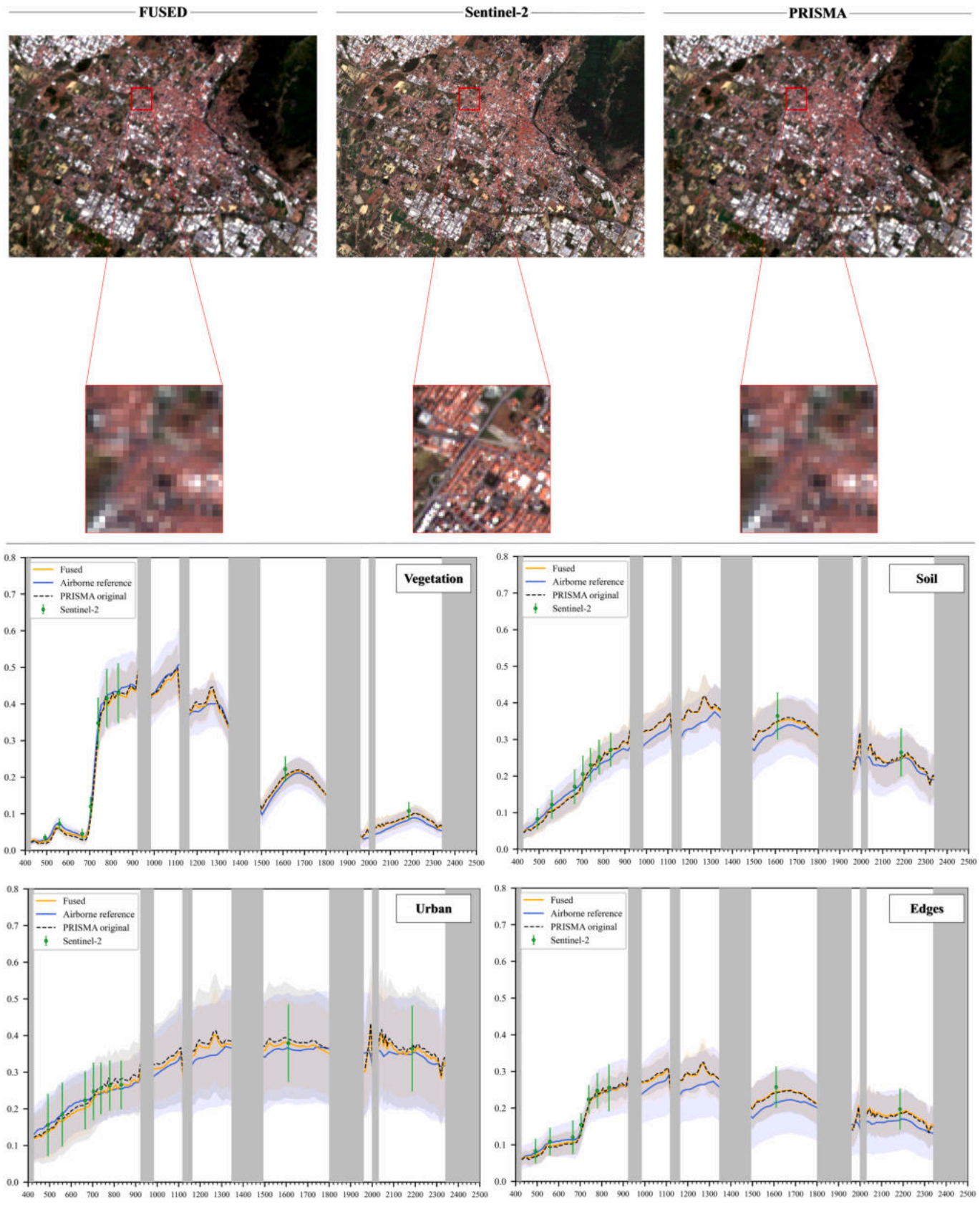

Fig. 8. Prato study area. On the top row: true color PRISMA fused image, as returned by HySure HS-MS fusing process (left); Sentinel-2 image (middle); original PRISMA HS image (right). On the bottom, the spectral signatures retrieved from the PRISMA fused and original, airborne reference and Sentinel-2 images are plotted, representing four representative land cover classes (vegetation, top-left; bare soil, top-right; urban, bottom-left; edges, bottom-right).

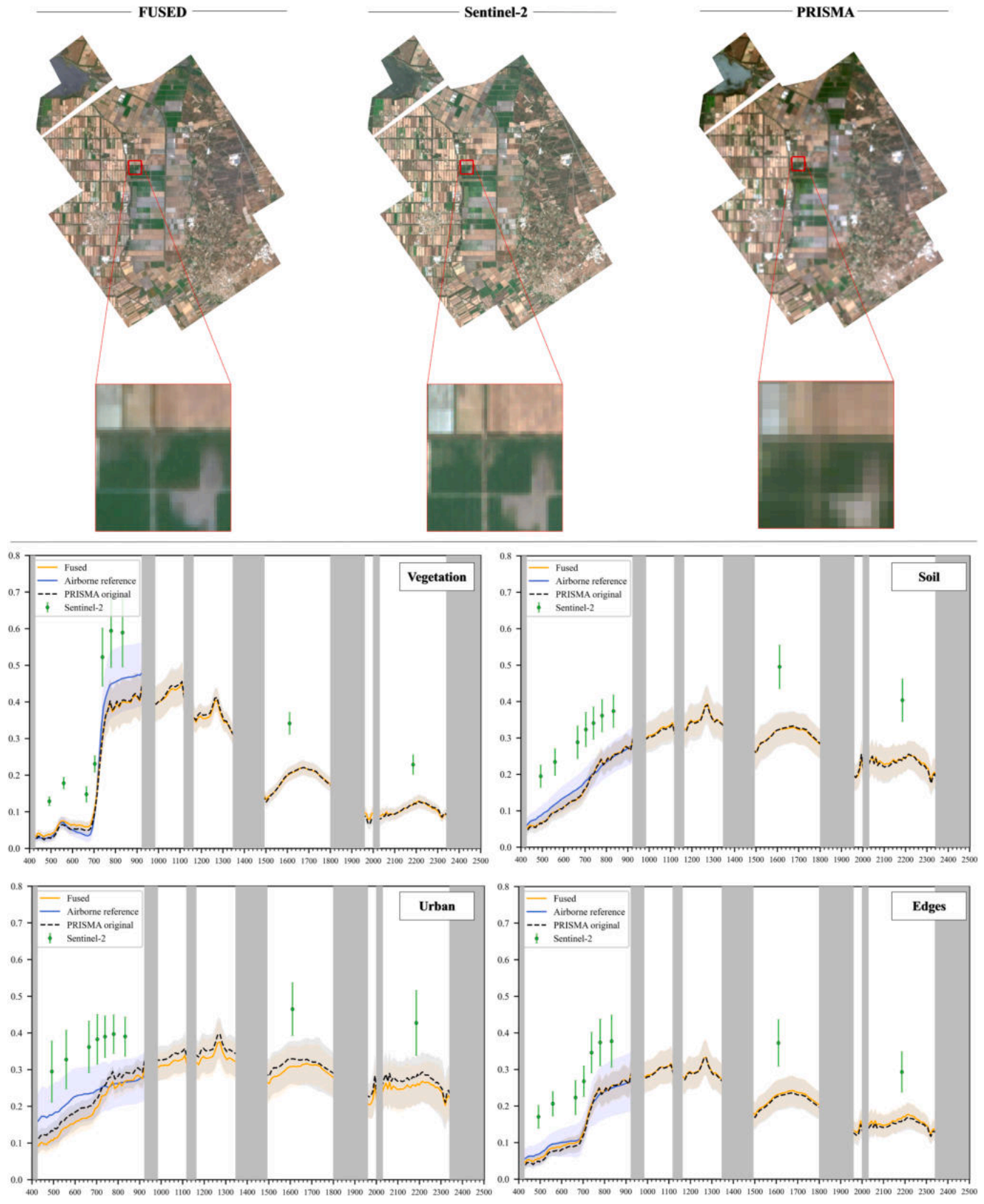

Fig. 9. Arborea study area. On the top row: true color PRISMA fused image, as returned by HySure HS-MS fusing process (left); Sentinel-2 image (middle); original PRISMA HS image (right). On the bottom, the spectral signatures retrieved from the PRISMA fused and original, airborne reference and Sentinel-2 images are plotted, representing four representative land cover classes (vegetation, top-left; bare soil, top-right; urban, bottom-left; edges, bottom-right).

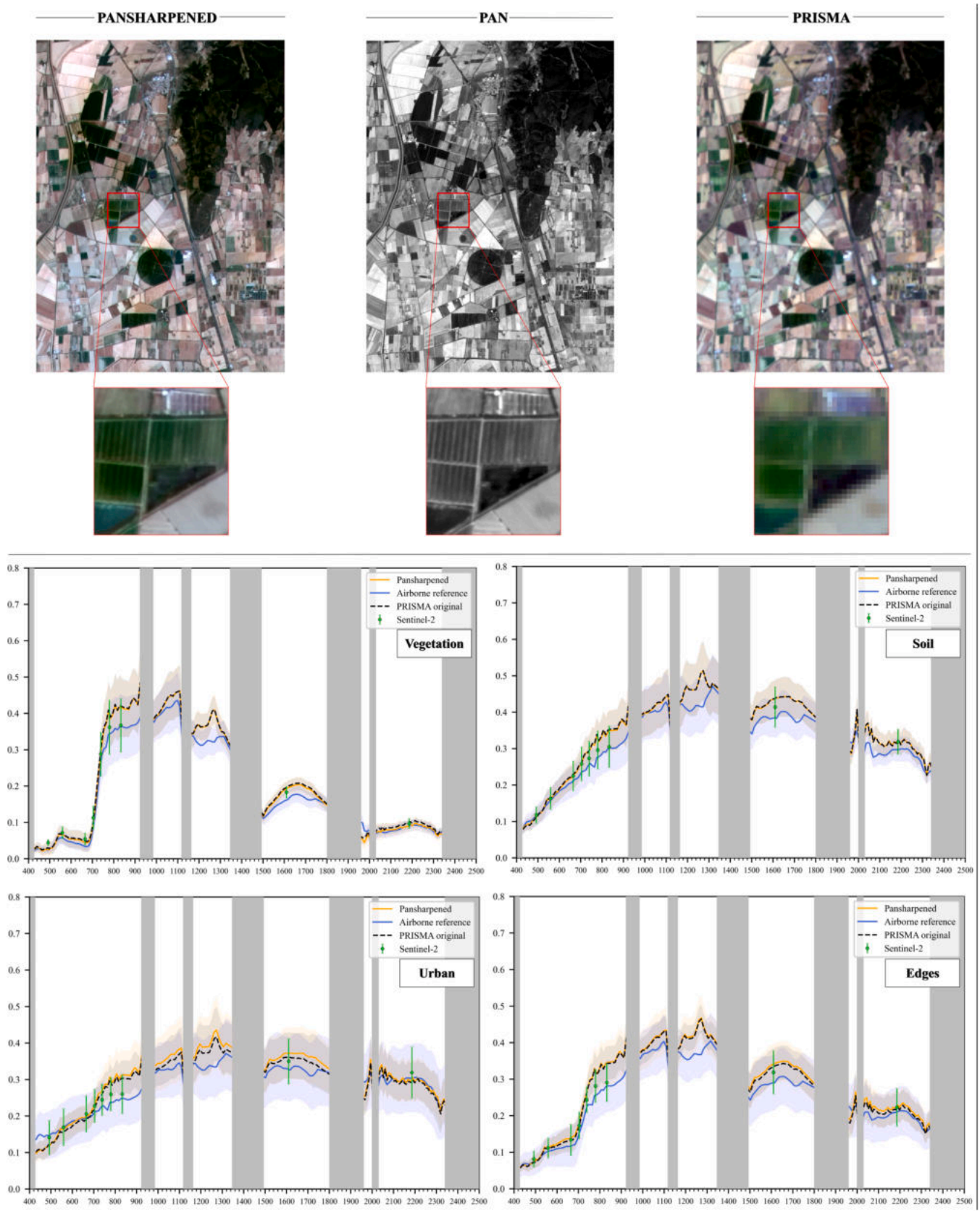

Fig. 10. Grosseto 0731 study area. On the top row: true color PRISMA fused image, as returned by HySure HS-PAN pansharpening process (left); PAN image (middle); original PRISMA HS image (right). On the bottom, the spectral signatures retrieved from the PRISMA pansharpened and original, airborne reference and Sentinel-2 images are plotted, representing four representative land cover classes (vegetation, top-left; bare soil, top-right; urban, bottom-left; edges, bottom-right).

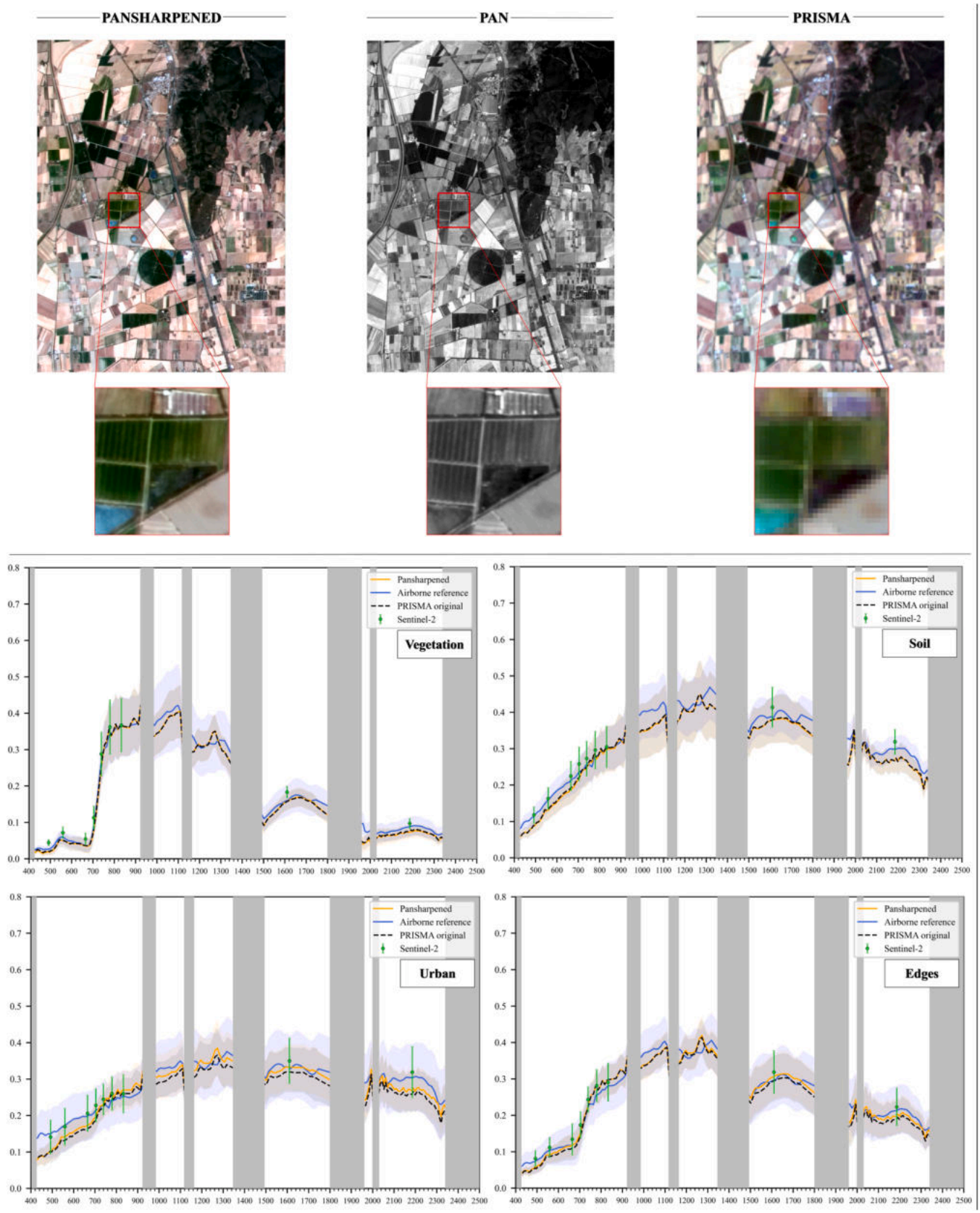

Fig. 11. Grosseto 0801 study area. On the top row: true color PRISMA fused image, as returned by HySure HS-PAN pansharpening process (left); PAN image (middle); original PRISMA HS image (right). On the bottom, the spectral signatures retrieved from the PRISMA pansharpened and original, airborne reference and Sentinel-2 images are plotted, representing four representative land cover classes (vegetation, top-left; bare soil, top-right; urban, bottom-left; edges, bottom-right).

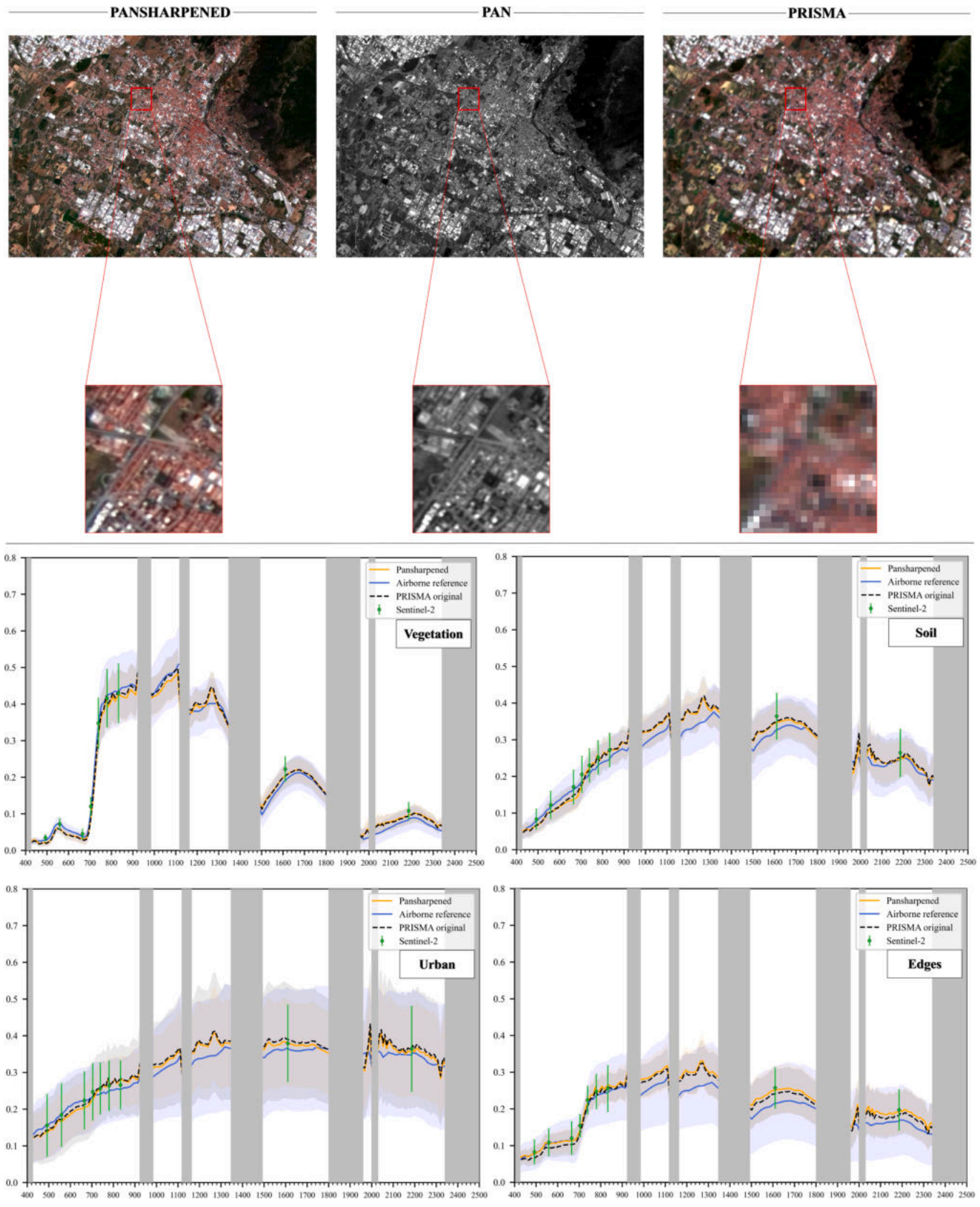

Fig. 12. Prato study area. On the top row: true color PRISMA fused image, as returned by HySure HS-PAN pansharpening process (left); PAN image (middle); original PRISMA HS image (right). On the bottom, the spectral signatures retrieved from the PRISMA pansharpened and original, airborne reference and Sentinel-2 images are plotted, representing four representative land cover classes (vegetation, top-left; bare soil, top-right; urban, bottom-left; edges, bottom-right).

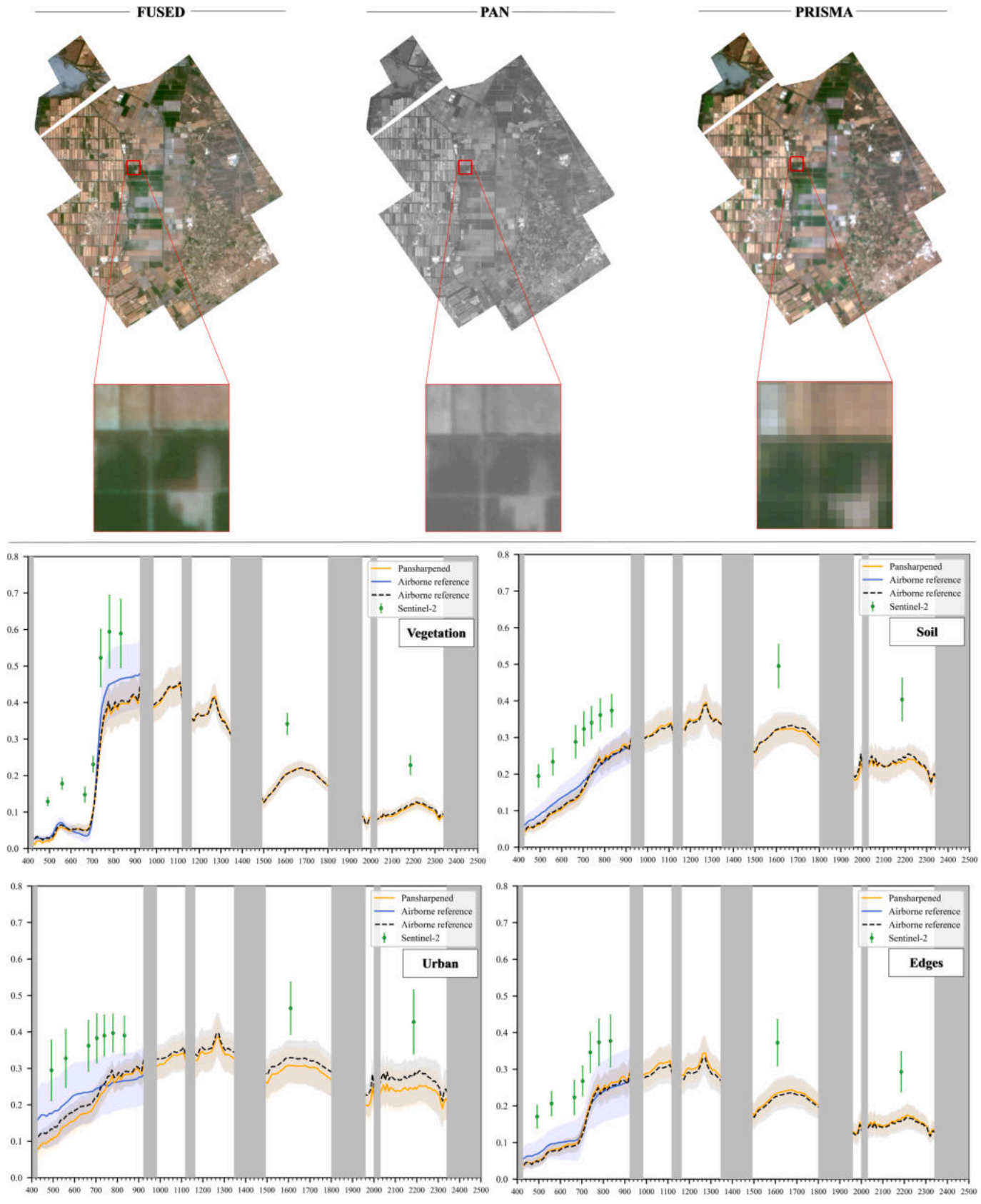

Fig. 13. Arborea study area. On the top row: true color PRISMA fused image, as returned by HySure HS-MS PAN pansharpening (left); PAN image (middle); original PRISMA HS image (right). On the bottom, the spectral signatures retrieved from the PRISMA pansharpened and original, airborne reference and Sentinel-2 images are plotted, representing four representative land cover classes (vegetation, top-left; bare soil, top-right; urban, bottom-left; edges, bottom-right).

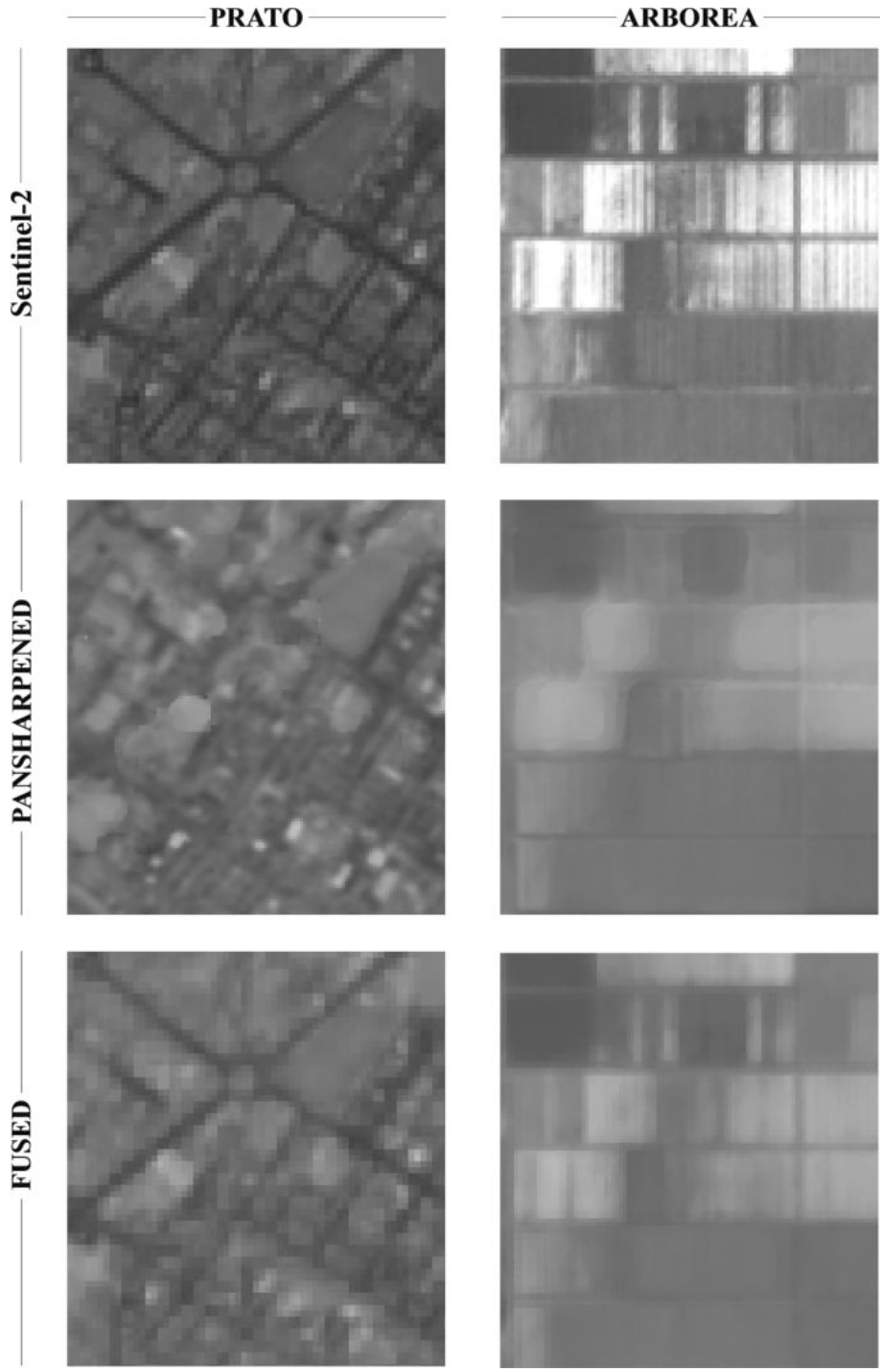

Fig. 14. Detailed overview focused on the blur artefacts present in some pansharpened (HS-PAN) PRISMA bands of Prato and Arborea study areas, compared to relative fused (HS-MS) and Sentinel-2 MS ones. The image band used as example is set on 950 nm (fused and pansharpened) and 833 nm (Sentinel-2).

In terms of computation demand, the process of HS-MS fusion took between 1800 and 2500 s to complete the 200 iterations per image with an Intel Core i7-12700 CPU running at 2.10 GHz with 16 GB of RAM, while time rises to 8000 s for pansharpening. Computation time is strictly dependent on image size, pixel size and number of iterations.

4. Discussion

4.1. Image co-registration

Finding an effective solution to address the PRISMA geometrical shift was necessary, due to the fast-growing demand by the EO-product providers (scientists, public agencies, industrial/business sector). The results of this study substantiated the declared geolocation accuracy of PRISMA imagery, with an average spatial error between 118 m and 170 m in all scenes, although it was found that the error is variable along the image (Figures S1-S5 in supplementary material). This precluded the use of models based on rigid displacements (first degree polynomial), in favour of a second-degree polynomial model to fully comply with the variable PRISMA shift. Similarly, Angelopoulou et al. (2023), enforced a manual selection of tie points on which a second-order polynomial model was applied to rectify the residual geometric shift to 1–2 pixels on

PRISMA images. Moreover, in AROSICS the correction was optimized using a moving window, in which an image portion is isolated from any surrounding high-distortion differences, allowing the local estimation of the shift and a more adequate transformation function.

When the co-registration is computed using single image pairs, it is expected that the advantages will be greater, as each slave image's irregularities are uniquely addressed (Barazzetti et al., 2014). Additionally, the composite process proposed in this study minimized residual errors raised during per-band image matching, ensuring higher-*reliability* tie point retrieval than comparing each pair of bands individually. Exception are the points in proximity to image edges, on water bodies, as already reported in the literature (Brotoisworo et al., 2022), and some residual randomly scattered across the scenes.

Often, if the time range between the target and the reference image is large, mismatches might arise due to variations at the surface, or due to changes in the solar angle (Chen and Jiang, 2021; Scaioni et al., 2018). The high temporal resolution of Sentinel-2 deals properly with this problem since most of the times close acquisition times to PRISMA's one is present.

Generally, in this study all the advantages claimed for AROSICS, namely the requirement of few input parameters, the possibility of managing multiple sensors, dealing with differences in reflectance, viewing geometry, acquisition mode and spatial resolution with no need for knowledge of remote system technical details and acquisition parameters, and the capability to return a point-based shapefile containing all the displacement statistics (e.g.: XY shift, *reliability*, etc.) were positively experienced.

4.2. Image fusion and pansharpening

Both HS-MS fusion and HS-PAN pansharpening yielded a satisfactory reconstruction of the spectral details in the improved-resolution PRISMA HS image, although the analyses reported here have demonstrated a superiority of the first approach compared to the second one. Still, the HS-MS outperformed pansharpening in reconstructing spatial patterns.

The reconstruction quality across the spectrum descripted by RMSEb, UIQIb and PSNRb metrics (Fig. 4) ascertains the robustness of the HS-MS fusion methodology in preserving the original spectral properties and minimize deformations, despite the divergence of Sentinel-2 in some regions of the spectrum (Figs. 6-13), which is substantial for those applications where the contribution of all – or of few but specific – bands, is required (Paris et al., 2019). This was confirmed by the comparison between spectral signatures of fusion/pansharpening outputs and original PRISMA (Figs. 6-13), from which it is hard to visually discern the differences between the original and the respective fused/pansharpened PRISMA's signatures. Overall color information performed also well, observing the three true color maps on the top of the same figures. On the other hand, this comparison raised that the spectral inconsistencies between the airborne reference data and the PRISMA satellite data were already present independently from the application of the HySure model, therefore not due to the fusion process. Actually, these cross-sensors discrepancies in PRISMA imagery were also found in Cogliati and coworkers (2021). Factors related to spectral resolution inconsistency between the two sensors should be excluded a priori: with a difference of central wavelength between PRISMA and airborne HS never exceeding 3 nm (CASI), 7 nm (SASI) and 2 nm (HySpex VNIR/SWIR), much lower than the respective FWHM, the spectral overlap was fully satisfied. Such difference was definitively minimized by the spectral resampling process. On the other hand, the divergencies observable in the VIS (especially on soil, urban and edges) and NIR regions (also on vegetation) might be partially related to the flawed parametrization of MODTRAN-5 model (airborne data correction), since the high sensitivity to the atmospheric scattering (especially blue region) (Niroumand-Jadidi et al., 2020; Pignatti et al., 2022). Concerning the comparison with Sentinel-2, Niroumand-Jadidi et al. (2020) also found some radiometric differences with PRISMA also in simultaneous acquisitions, possible attributable to other various factors that are not easily controllable, such as differences in the atmospheric correction, different noise patterns, sensor sensitivity. The same authors also deduced that the atmospheric path radiance (VNIR) is slightly underestimated in PRISMA level 2D products, especially at short-wavelength bands (442 nm and 492 nm) if compared to Sentinel-2 spectrum. Actually, spectral fidelity issues affecting PRISMA's blue bands are well-known, raising within PRISCAV experiments (e.g. Pellegrino et al. 2023; Braga et al. 2022). However, it must be taken into account that the PRISMA atmospheric correction processor is continuously updated, which leads to growing improvements in radiometric artefacts presence. Further investigation should be invested in this sense, for example by harmonizing the atmospheric correction across all the adopted sensors. This might be easily applied operationally thanks to the availability of highly-versatile software, such as the MODTRAN-based ImaACor (Palombo and Santini, 2020), which already includes several utilities for PRISMA and Sentinel-2 pre-processing, as well as being already tested on CASI imagery.

Besides the bias between cross-sensor signatures comparison, the resulted overall accuracy metrics values expressed very satisfying performances, in line with optimal values presented in literature (Acito et al., 2022; Dian et al., 2021; Lanaras et al., 2017; Wang et al., 2021). Considering only pansharpened outputs, the quantitative results achieved in our analysis are equal to, or even superior (UIQI for Prato and Grosseto study areas) the baselines proposed in the WHISPERS 2022 competition (Vivone et al., 2023).

The presented methodology returned a large number of pixels with low reconstruction errors, largely for HS-MS fusion outputs. The spatial distribution of reconstruction error, observable in the RMSEp and SAMp maps (Fig. 5) shows higher magnitude at slim shapes, single patches geometries and edge/transition between different land covers (roads, buildings, etc.) in outputs coming from pansharpening, while the fusion approach minimized the spatial errors on this type of geometries, preserving texture and internal/external edge details. The error magnitude is in general more conspicuous in the urban area of Prato, but on the other hand this was expected and commonly found in literature since those are spatial features difficult to remodel (Veganzones et al., 2016). This could be due to the higher homogeneity of vegetation and soil components inside pixels, compared to the more complex texture of the urban land cover (red tiles roofs, asphalt, streets, metal roofs, solar panel, etc.). Nevertheless, the error values still contained even in the urban scenario corroborate what other authors (Brezini and Deville, 2023) found out, concerning the reduced spatial distortion and a better spatial fidelity for the urban area provided by HySure compared to the other experimented fusion methods. At the same time, pansharpening outputs returned unclear blurred artefacts and inconsistent edge details in some bands of the IR domain (only in Arborea and Prato areas). This type of artifact is not the first time it has been encountered when trying to apply pansharpening to PRISMA images. Kremizi et al. (2021) observed blurring and duplicative edges after having tested different pansharpening approaches, including deep learning, attributing them to the injection of high-pass details, probably emphasized by incorrect registration between the HS and PAN data. Acito et al. (2022) supposed that such blurring artefacts are also attributable to residual coregistration bias. In the present work, a HS-PAN misalignment was not taken into account since both the manufacturer's technical notes (ASI - Agenzia Spaziale Italiana, 2020) and visual inspections confirmed the effective spatial matching between HS and PAN in PRISMA. Regarding the HS-MS fusion process, Acito et al. (2022) found that the impact of minimum residual coregistration errors on PRISMA and Sentintel-2 fusion was negligeable, also including experimental tests on HySure.

Furthermore, the role played by the resolution ratio between PRISMA HS and Sentinel-2 GSDs should be accounted for. A more cautious reduction in the resolution of the raw data, in terms of low ratio between the original GSD and the expected improved GSD, is more efficient in preserving spatial information and minimizing distortions

than when the GSD ratios are higher (e.g. > 4), such as between PRISMA HS and PAN data (Dian et al., 2021; Fu et al., 2019; Vaiopoulos and Karantzalos, 2016). These kinds of issues were experienced also by Vivone et al. (2023) in the pansharpening of PRISMA images. Kremezi et al. (2021), again, suspected that their pansharpening results of PRISMA were negatively largely affected also by the high difference in spatial detail contained in the pixels of HS and PAN datasets, as well as the presence of linear periodic noise in the PAN image. In this last regard, there is still no definitive evidence about the contribution of noise (and the impact of denoising processes) to image fusion. This topic needs to be further investigated, since PRISMA is affected by both random and fixed noise pattern (Carfora et al., 2022; Pignatti et al., 2022). Further investigation is required also to understand the influence of topographical complexity on sensor backscatter and SNR (Vangi et al., 2021). In the present case, some very noised PRISMA bands were excluded (Section 2.1.1) but, through preliminary visual tests (not reported), it was observed that the contribution given by the MS information managed to minimize the noise in the HS-MS fusion outputs also when the badly noised bands were kept. Similar results were also reported in Lanaras et al. (2017) after adopting an unmixing-based fusion algorithm. Acito et al. (2022) observed that HySure expresses low noise sensitivity, attributable to its effective modeling of spectral redundancies and similarities making use of the subspace projection and the VTV regularization (Dian et al., 2021). Yokoya et al. (2017) attributed the superior performance of HySure just to the denoising process integrated in its processes. Artifacts in the fusion images are, however, generally expected according to (Acito et al., 2022; Dian et al., 2018; Lanaras et al., 2017) and, in our opinion, they shouldn't cause strong concerns if they remain few and weak, since much still needs to be done to optimize these algorithms.

An actual limitation could be given by the computational efficiency and high memory consumption of the HySure model, which is typical for matrix factorization algorithms, especially if they need to solve the complex optimization problem iteratively (Dian et al., 2021; Sara et al., 2021; Selva et al., 2015; Wang et al., 2021). This specific question was not yet fulfilled, as also requested in WHISPER 2022 (Vivone et al., 2023). However, the free availability of the code would allow an improvement in this sense.

5. Conclusions

In the present study, the two processes of HS-MS fusion and HS-PAN pansharpening were implemented and compared to improve the spatial resolution of PRISMA images, precursor of the next-generation European HS satellites. The two processes involved the Sentinel-2 MS data and the PRISMA PAN respectively. The experiments were conducted with the well-known HySure model, considered a scientific baseline among image fusion methods for its cutting-edge performance, also extendable to pansharpening approaches. Three different land use distributions, within rural and urban landscapes, were examined, on which the sharpening quality was quantitatively evaluated by computation of *ad-hoc* validation metrics using airborne HS images as reference. In terms of accuracy of improved PRISMA HS, the fusion outperformed the pansharpening method in retaining both spectral and spatial information, due to the positive contribution of the MS Sentinel 2 spectrum. Although pansharpening enabled the achievement of 5 m GSD, the HS-MS fusion outputs (10 m GSD) was more suited to resolve spatial heterogeneity, especially important in urban areas such as Prato, avoiding any severe blur and at-edge artefact that were, instead, observed in HS-PAN pansharpening.

Sentinel-2 data has proven to be effective also as an accurate geometric reference to estimate the spatial displacement and perform the semi-automatic geo-correction of PRISMA imagery. The experimental results demonstrated that the X/Y shift of PRISMA was, on average, around 150 m, with peaks of 200–250 m, and its spatial distribution was not consistent between one study area and another. Magnitude and directions of the shift were not constant across the scene (supplementary material) and resulted in the need to apply a second order polynomial function to optimize the image correction.

Although the temporal gap between multi-source acquisitions of the same scene may not favor optimal spectral affinity between ground features, as well affecting the co-registration process due to possible land use changes that have occurred in the meantime, the high temporal resolution of Sentinel-2 prevented this issue.

Additional tests should be also carried out in challenging landscapes, such as rough and sloping mountainous areas, high-albedo snowed areas, water surfaces, etc. In those contexts, a specific analysis should be applied due the complex and dynamical reflective behaviors, to which both co-registration and fusion processed are highly sensitive. Even greater attention must be paid to the analysis of water bodies. Both co-registration by-products and fusion/pansharpening accuracy (SAMp) showed high levels of error on this surface, probably associated with the low spectral response of the water (Veganzones et al., 2016), with its higher cross-sensor sensitivity (Giardino et al., 2020), and/or with other several optical properties of (Alicandro et al., 2022).

We conclude that the combination of the two state-of-the-art tools, AROSICS and HySure, adopting both spatial and spectral information of the free-available and high temporal resolution Sentinel-2 data, can successfully resolve both the geometric displacement correction and the spatial resolution improvement of PRISMA HS imagery. It is worth mentioning that the code for both tools is easily available, and althought HySure is built in the closed-source MATLAB language, the code itself is provided free of charge and can be easily translatable to other open-source languages (such as Python). Given the sensitivity of fusion process to the correct SRF selection, the relative SRF and PSF auto-estimation capacity is a very strong point of HySure, enabling it to maximizee the reconstruction accuracy. This process might not be immune to critical issues, already reported in literature. In our opinion, the implementation of a trial-and-error approach for optimizing the regularization parameters (λ_R and λ_B), is an efficient method to adapt this process to the observed scene.

These characteristics are crucial for operational purposes, allowing a wide range of users to improve and fully exploit the whole set of HS information available in the framework of EO. Considering the list of upcoming European HS satellites (e.g., ESA CHIME; Spaceborne Hyperspectral Applicative Land and Ocean Mission, SHALOM; and ASI PRISMA-2), and currently competing with other constellations (EU and extra-EU) at different stages of development (Qian, 2021), whose fine spectral information will be fundamental in many environmental applications of growing interest, we believe that the analysis performed on PRISMA HS will provide useful information for further exploitation of co-registration and pansharpening/fusion approaches in HS remote sensing.

Credit authorship contribution statement

Giandomenico De Luca: Writing – review & editing, Writing – original draft, Visualization, Validation, Software, Methodology, Investigation, Formal analysis, Data curation, Conceptualization. **Federico Carotenuto:** Writing – review & editing, Software, Methodology, Formal analysis, Data curation. **Lorenzo Genesio:** Writing – review & editing, Supervision, Resources, Project administration, Funding acquisition, Conceptualization. **Monica Pepe:** Writing – review & editing. **Piero Toscano:** Writing – review & editing. **Mirco Boschetti:** Writing – review & editing, Funding acquisition. **Franco Miglietta:** Supervision. **Beniamino Gioli:** Writing – review & editing, Supervision, Resources, Project administration, Funding acquisition, Conceptualization.

Declaration of competing interest

The authors declare that they have no known competing financial

interests or personal relationships that could have appeared to influence the work reported in this paper.

Acknowledgements

Authors' contribution is distributed as follows: conceptualization by G.D., L.G. and B.G.; investigation by G.D.; methodology by G.D. and F.C.; formal analysis by G.D. and F.C.; data curation by G.D. and F.C.; software by G.D. and F.C.; validation by G.D.; visualization by G.D.; original draft writing and preparation by G.D.; writing, proof reviewing and editing by all the authors.

This study made use of PRISMA Products of the Italian Space Agency (ASI), delivered under an ASI License to use, and was made possible by the funding support of: the agreement ASI-CNR, n. 20195HH0 "Attività scientifica di CAL/VAL della missione PRISMA - PRISCAV"; the projects "E-crops—Tecnologie per l'Agricoltura Digitale Sostenibile" (PON Ricerca e Innovazione 2014–2020, ARS01_01136) and "Agro-Sensing" (CNR FOE 2020). We thank Ilaria Tabarrani (Regione Toscana) for coordinating the HS flight measurements in Prato, and Andrea Genangeli for ground support during the flights.

Appendix A. Supplementary data

Supplementary data to this article can be found online at https://doi.org/10.1016/j.isprsjprs.2024.07.003.

References

Acito, N., Diani, M., Corsini, G., 2022. PRISMA Spatial Resolution Enhancement by Fusion With Sentinel-2 Data. IEEE J Sel Top Appl Earth Obs Remote Sens 15, 62–79. https://doi.org/10.1109/JSTARS.2021.3132135.

Alicandro, M., Candigliota, E., Dominici, D., Immordino, F., Masin, F., Pascucci, N., Quaresima, R., Zollini, S., 2022. Hyperspectral PRISMA and Sentinel-2 Preliminary Assessment Comparison in Alba Fucens and Sinuessa Archaeological Sites (Italy). Land (basel) 11. https://doi.org/10.3390/land11112070.

Amieva, J.F., Oxoli, D., Brovelli, M.A., 2023. Machine and Deep Learning Regression of Chlorophyll-a Concentrations in Lakes Using PRISMA Satellite Hyperspectral Imagery. Remote Sens (basel). https://doi.org/10.3390/rs15225385.

Angelopoulou, T., Chabrillat, S., Pignatti, S., Milewski, R., Karyotis, K., Brell, M., Ruhtz, T., Bochtis, D., Zalidis, G., 2023. Evaluation of Airborne HySpex and Spaceborne PRISMA Hyperspectral Remote Sensing Data for Soil Organic Matter and Carbonates Estimation. Remote Sens (basel) 15. https://doi.org/10.3390/rs15041106.

Asi, 2020. Agenzia Spaziale Italiana. PRISMA Products Specification Document.

Barazzetti, L., Scaioni, M., Gianinetto, M., 2014. Automatic Co-registration of Satellite Time Series via Least Squares Adjustment. Eur J Remote Sens 47, 55–74. https://doi.org/10.5721/EuJRS20144705.

Bay, H., Ess, A., Tuytelaars, T., Van Gool, L., 2008. Speeded-Up Robust Features (SURF). Computer Vision and Image Understanding 110, 346–359. https://doi.org/10.1016/j.cviu.2007.09.014.

Bohn, N., Di Mauro, B., Colombo, R., Thompson, D.R., Susiluoto, J., Carmon, N., Turmon, M.J., Guanter, L., 2022. Glacier Ice Surface Properties in South-West Greenland Ice Sheet: First Estimates From PRISMA Imaging Spectroscopy Data. J Geophys Res Biogeosci 127, e2021JG006718. https://doi.org/10.1029/2021JG006718.

Bracewell, R., Kahn, P.B., 1966. The Fourier Transform and Its Applications. Am J Phys 34, 712. https://doi.org/10.1119/1.1973431.

Braga, F., Fabbretto, A., Vanhellemont, Q., Bresciani, M., Giardino, C., Scarpa, G.M., Manfè, G., Concha, J.A., Brando, V.E., 2022. Assessment of PRISMA water reflectance using autonomous hyperspectral radiometry. ISPRS Journal of Photogrammetry and Remote Sensing 192, 99–114. https://doi.org/10.1016/j.isprsjprs.2022.08.009.

Bresson, X., Chan, T.F., 2008. Fast dual minimization of the vectorial total variation norm and applications to color image processing. Inverse Problems and Imaging 2, 455–484. https://doi.org/10.3934/ipi.2008.2.455.

Brezini, S.E., Deville, Y., 2023. Hyperspectral and Multispectral Image Fusion with Automated Extraction of Image-Based Endmember Bundles and Sparsity-Based Unmixing to Deal with Spectral Variability. Sensors. https://doi.org/10.3390/s23042341.

Brotoisworo, P., Aranas, R.K., Felix, M.J., 2022. Automated georeferencing of Diwata-2 multispectral imagery using feature matching. J Phys Conf Ser 2214, 12027. https://doi.org/10.1088/1742-6596/2214/1/012027.

Carfora, M.F., Casa, R., Laneve, G., Mzid, N., Pascucci, S., Pignatti, S., 2022. Prisma Noise Coefficients Estimation, in: IGARSS 2022 - 2022 IEEE International Geoscience and Remote Sensing Symposium. pp. 7531–7534. Doi: 10.1109/IGARSS46834.2022.9883584.

Chen, Y., Jiang, J., 2021. A Two-Stage Deep Learning Registration Method for Remote Sensing Images Based on Sub-Image Matching. Remote Sens (basel). https://doi.org/10.3390/rs13173443.

Cogliati, S., Sarti, F., Chiarantini, L., Cosi, M., Lorusso, R., Lopinto, E., Miglietta, F., Genesio, L., Guanter, L., Damm, A., Pérez-López, S., Scheffler, D., Tagliabue, G., Panigada, C., Rascher, U., Dowling, T.P.F., Giardino, C., Colombo, R., 2021. The PRISMA imaging spectroscopy mission: overview and first performance analysis. Remote Sens Environ 262, 112499. https://doi.org/10.1016/j.rse.2021.112499.

De Gregorio, L., Callegari, M., Colombo, R., Cremonese, E., Mauro, B. Di, Garzonio, R., Giardino, C., Marin, C., Matta, E., Notarnicola, C., Pepe, M., Ravasio, C., Montuori, A., Licciardi, G., 2023. SCIA Project: Development of Algorithms for Generating Products Related to Cryosphere by Exploiting PRISMA Hyperspectral Data, in: IGARSS 2023 - 2023 IEEE International Geoscience and Remote Sensing Symposium. pp. 1641–1643. Doi: 10.1109/IGARSS52108.2023.10283123.

Dian, R., Li, S., Guo, A., Fang, L., 2018. Deep Hyperspectral Image Sharpening. IEEE Trans Neural Netw Learn Syst 29, 5345–5355. https://doi.org/10.1109/TNNLS.2018.2798162.

Dian, R., Li, S., Sun, B., Guo, A., 2021. Recent advances and new guidelines on hyperspectral and multispectral image fusion. Information Fusion 69, 40–51. https://doi.org/10.1016/j.inffus.2020.11.001.

ESA Snap Cookbook, 2024. ESA SNAP Cookbook [WWW Document]. accessed 4.21.24. https://senbox.atlassian.net/wiki/spaces/SNAP/pages/24051769/Cookbook.

Foroosh, H., Zerubia, J.B., Berthod, M., 2002. Extension of phase correlation to subpixel registration. IEEE Transactions on Image Processing 11, 188–200. https://doi.org/10.1109/83.988953.

Frigo, M., Johnson, S.G., 1997. The Fastest Fourier Transform in the West (MIT-LCS-TR-728).

Frigo, M., Johnson, S.G., 2005. The Design and Implementation of FFTW3. Proceedings of the IEEE 93, 216–231. https://doi.org/10.1109/JPROC.2004.840301.

Fu, Y., Zhang, T., Zheng, Y., Zhang, D., Huang, H., 2019. Hyperspectral Image Super-Resolution With Optimized RGB Guidance, in: 2019 IEEE/CVF Conference on Computer Vision and Pattern Recognition (CVPR). pp. 11653–11662. Doi: 10.1109/CVPR.2019.01193.

Gdal, 2024. GDAL documentation [WWW Document]. accessed 1.31.24. https://gdal.org/index.html.

Gianinetto, M., Scaioni, M., 2008. Automated Geometric Correction of High-resolution Pushbroom Satellite Data. Photogramm Eng Remote Sensing 74, 107–116. https://doi.org/10.14358/PERS.74.1.107.

Giardino, C., Bresciani, M., Braga, F., Fabbretto, A., Ghirardi, N., Pepe, M., Gianinetto, M., Colombo, R., Cogliati, S., Ghebrehiwot, S., Laanen, M., Peters, S., Schroeder, T., Concha, J.A., Brando, V.E., 2020. First Evaluation of PRISMA Level 1 Data for Water Applications. Sensors. https://doi.org/10.3390/s20164553.

Guanter, L., Irakulis-Loitxate, I., Gorroño, J., Sánchez-García, E., Cusworth, D.H., Varon, D.J., Cogliati, S., Colombo, R., 2021. Mapping methane point emissions with the PRISMA spaceborne imaging spectrometer. Remote Sens Environ 265, 112671. https://doi.org/10.1016/j.rse.2021.112671.

Guarini, R., Loizzo, R., Facchinetti, C., Longo, F., Ponticelli, B., Faraci, M., Dami, M., Cosi, M., Amoruso, L., Pasquale, V. De, Taggio, N., Santoro, F., Colandrea, P., Miotti, E., Nicolantonio, W. Di, 2018. Prisma Hyperspectral Mission Products, in: IGARSS 2018 - 2018 IEEE International Geoscience and Remote Sensing Symposium. pp. 179–182. Doi: 10.1109/IGARSS.2018.8517785.

He, W., Hong, D., Scarpa, G., Uezato, T., Yokoya, N., 2021. Multisource Remote Sensing Image Fusion. Deep Learning for the Earth Sciences. 136–149. https://doi.org/10.1002/9781119646181.ch10.

Inamdar, D., Kalacska, M., Leblanc, G., Arroyo-Mora, J.P., 2020. Characterizing and mitigating sensor generated spatial correlations in airborne hyperspectral imaging data. Remote Sens (basel) 12. https://doi.org/10.3390/rs12040641.

Kremezi, M., Kristollari, V., Karathanassi, V., Topouzelis, K., Kolokoussis, P., Taggio, N., Aiello, A., Ceriola, G., Barbone, E., Corradi, P., 2021. Pansharpening PRISMA Data for Marine Plastic Litter Detection Using Plastic Indexes. IEEE Access 9, 61955–61971. https://doi.org/10.1109/ACCESS.2021.3073903.

Lanaras, C., Baltsavias, E., Schindler, K., 2017. Hyperspectral Super-Resolution with Spectral Unmixing Constraints. Remote Sens (basel). https://doi.org/10.3390/rs9111196.

Li, J., Hong, D., Gao, L., Yao, J., Zheng, K., Zhang, B., Chanussot, J., 2022. Deep learning in multimodal remote sensing data fusion: A comprehensive review. International Journal of Applied Earth Observation and Geoinformation 112, 102926. https://doi.org/10.1016/j.jag.2022.102926.

Loizzo, R., Daraio, M., Guarini, R., Longo, F., Lorusso, R., Dini, L., Lopinto, E., 2019. Prisma Mission Status and Perspective, in. In: IGARSS 2019–2019 IEEE International Geoscience and Remote Sensing Symposium, pp. 4503–4506. https://doi.org/10.1109/IGARSS.2019.8899272.

Long, T., Jiao, W., He, G., Zhang, Z., 2016. A Fast and Reliable Matching Method for Automated Georeferencing of Remotely-Sensed Imagery. Remote Sens (basel). https://doi.org/10.3390/rs8010056.

Lowe, D.G., 1999. Object recognition from local scale-invariant features, in: Proceedings of the Seventh IEEE International Conference on Computer Vision. pp. 1150–1157 vol.2. Doi: 10.1109/ICCV.1999.790410.

Niroumand-Jadidi, M., Bovolo, F., Bruzzone, L., 2020. Water Quality Retrieval from PRISMA Hyperspectral Images: First Experience in a Turbid Lake and Comparison with Sentinel-2. Remote Sens (basel). https://doi.org/10.3390/rs12233984.

Online, S., 2021. Forthcoming deployment of the Copernicus Sentinel-2 products geometric refinement [WWW Document]. accessed 1.31.24. https://sentinels.copernicus.eu/web/sentinel/-/forthcoming-deployment-of-the-copernicus-sentinel-2-products-geometric-refinement.

Otazu, X., Gonzalez-Audicana, M., Fors, O., Nunez, J., 2005. Introduction of sensor spectral response into image fusion methods. Application to wavelet-based methods. IEEE Transactions on Geoscience and Remote Sensing 43, 2376–2385. https://doi.org/10.1109/TGRS.2005.856106.

Palombo, A., Santini, F., 2020. ImaACor: A Physically Based Tool for Combined Atmospheric and Topographic Corrections of Remote Sensing Images. Remote Sens (basel) 12. https://doi.org/10.3390/rs12132076.

Paris, C., Bioucas-Dias, J., Bruzzone, L., 2019. A Novel Sharpening Approach for Superresolving Multiresolution Optical Images. IEEE Transactions on Geoscience and Remote Sensing 57, 1545–1560. https://doi.org/10.1109/TGRS.2018.2867284.

Pellegrino, A., Fabbretto, A., Bresciani, M., de Lima, T.M., Braga, F., Pahlevan, N., Brando, V.E., Kratzer, S., Gianinetto, M., Giardino, C., 2023. Assessing the Accuracy of PRISMA Standard Reflectance Products in Globally Distributed Aquatic Sites. Remote Sens (basel). https://doi.org/10.3390/rs15082163.

Pepe, M., Pompilio, L., Gioli, B., Busetto, L., Boschetti, M., 2020. Detection and Classification of Non-Photosynthetic Vegetation from PRISMA Hyperspectral Data in Croplands. Remote Sens (basel). https://doi.org/10.3390/rs12233903.

Pepe, M., Pompilio, L., Ranghetti, L., Nutini, F., Boschetti, M., 2023. Mapping spatial distribution of crop residues using PRISMA satellite imaging spectroscopy. Eur J Remote Sens 56, 2122872. https://doi.org/10.1080/22797254.2022.2122872.

Pignatti, S., Amodeo, A., Carfora, M.F., Casa, R., Mona, L., Palombo, A., Pascucci, S., Rosoldi, M., Santini, F., Laneve, G., 2022. PRISMA L1 and L2 Performances within the PRISCAV Project: The Pignola Test Site in Southern Italy. Remote Sens (basel) 14. https://doi.org/10.3390/rs14091985.

Pignatti, S., Palombo, A., Pascucci, S., Romano, F., Santini, F., Simoniello, T., Umberto, A., Vincenzo, C., Acito, N., Diani, M., Matteoli, S., Corsini, G., Casa, R., Bonis, R. De, Laneve, G., Ananasso, C., 2013. The PRISMA hyperspectral mission: Science activities and opportunities for agriculture and land monitoring, in: 2013 IEEE International Geoscience and Remote Sensing Symposium - IGARSS. pp. 4558–4561. Doi: 10.1109/IGARSS.2013.6723850.

Qian, S.-E., 2021. Hyperspectral Satellites, Evolution, and Development History. IEEE J Sel Top Appl Earth Obs Remote Sens 14, 7032–7056. https://doi.org/10.1109/JSTARS.2021.3090256.

Qu, Y., Qi, H., Kwan, C., Yokoya, N., Chanussot, J., 2022. Unsupervised and Unregistered Hyperspectral Image Super-Resolution With Mutual Dirichlet-Net. IEEE Transactions on Geoscience and Remote Sensing 60, 1–18. https://doi.org/10.1109/TGRS.2021.3079518.

Quintano, C., Calvo, L., Fernández-Manso, A., Suárez-Seoane, S., Fernandes, P.M., Fernández-Guisuraga, J.M., 2023. First evaluation of fire severity retrieval from PRISMA hyperspectral data. Remote Sens Environ 295, 113670. https://doi.org/10.1016/j.rse.2023.113670.

Sara, D., Mandava, A.K., Kumar, A., Duela, S., Jude, A., 2021. Hyperspectral and multispectral image fusion techniques for high resolution applications: a review. Earth Sci Inform 14, 1685–1705. https://doi.org/10.1007/s12145-021-00621-6.

Scaioni, M., Barazzetti, L., Gianinetto, M., 2018. Multi-Image Robust Alignment of Medium-Resolution Satellite Imagery. Remote Sens (basel). https://doi.org/10.3390/rs10121969.

Scheffler, D., Hollstein, A., Diedrich, H., Segl, K., Hostert, P., 2017. AROSICS: An Automated and Robust Open-Source Image Co-Registration Software for Multi-Sensor Satellite Data. Remote Sens (basel). https://doi.org/10.3390/rs9070676.

Selva, M., Aiazzi, B., Butera, F., Chiarantini, L., Baronti, S., 2015. Hyper-Sharpening: A First Approach on SIM-GA Data. IEEE J Sel Top Appl Earth Obs Remote Sens 8, 3008–3024. https://doi.org/10.1109/JSTARS.2015.2440092.

Simões, M., Bioucas-Dias, J., Almeida, L.B., Chanussot, J., 2014. Hyperspectral image superresolution: An edge-preserving convex formulation. In: In: 2014 IEEE International Conference on Image Processing (ICIP), pp. 4166–4170. https://doi.org/10.1109/ICIP.2014.7025846.

Simões, M., Bioucas-Dias, J., Almeida, L.B., Chanussot, J., 2015. A Convex Formulation for Hyperspectral Image Superresolution via Subspace-Based Regularization. IEEE Transactions on Geoscience and Remote Sensing 53, 3373–3388. https://doi.org/10.1109/TGRS.2014.2375320.

Skakun, S., Roger, J.-C., Vermote, E.F., Masek, J.G., Justice, C.O., 2017. Automatic sub-pixel co-registration of Landsat-8 Operational Land Imager and Sentinel-2A Multi-Spectral Instrument images using phase correlation and machine learning based mapping. Int J Digit Earth 10, 1253–1269. https://doi.org/10.1080/17538947.2017.1304586.

Stumpf, A., Michéa, D., Malet, J.-P., 2018. Improved Co-Registration of Sentinel-2 and Landsat-8 Imagery for Earth Surface Motion Measurements. Remote Sens (basel). https://doi.org/10.3390/rs10020160.

Vaiopoulos, A.D., Karantzalos, K., 2016. PANSHARPENING ON THE NARROW VNIR AND SWIR SPECTRAL BANDS OF SENTINEL-2. Int. Arch. Photogramm. Remote Sens. Spatial Inf. Sci. XLI-B7, 723–730. https://doi.org/10.5194/isprs-archives-XLI-B7-723-2016.

Vakalopoulou, M., Christodoulidis, S., Sahasrabudhe, M., Mougiakakou, S., Paragios, N., 2019. Image Registration of Satellite Imagery with Deep Convolutional Neural Networks. In: In: IGARSS 2019–2019 IEEE International Geoscience and Remote Sensing Symposium, pp. 4939–4942. https://doi.org/10.1109/IGARSS.2019.8898220.

Vangi, E., D'Amico, G., Francini, S., Giannetti, F., Lasserre, B., Marchetti, M., Chirici, G., 2021. The New Hyperspectral Satellite PRISMA: Imagery for Forest Types Discrimination. Sensors. https://doi.org/10.3390/s21041182.

Vavassori, A., Giuliani, G., Brovelli, M.A., 2023. Mapping Local Climate Zones in Lausanne (Switzerland) with Sentinel-2 and PRISMA imagery: comparison of classification performance using different band combinations and building height data. Int J Digit Earth 16, 4790–4810. https://doi.org/10.1080/17538947.2023.2283485.

Veganzones, M.A., Simões, M., Licciardi, G., Yokoya, N., Bioucas-Dias, J.M., Chanussot, J., 2016. Hyperspectral Super-Resolution of Locally Low Rank Images From Complementary Multisource Data. IEEE Transactions on Image Processing 25, 274–288. https://doi.org/10.1109/TIP.2015.2496263.

Vivone, G., 2023. Multispectral and hyperspectral image fusion in remote sensing: A survey. Information Fusion 89, 405–417. https://doi.org/10.1016/j.inffus.2022.08.032.

Vivone, G., Mura, M.D., Garzelli, A., Restaino, R., Scarpa, G., Ulfarsson, M.O., Alparone, L., Chanussot, J., 2021. A New Benchmark Based on Recent Advances in Multispectral Pansharpening: Revisiting Pansharpening With Classical and Emerging Pansharpening Methods. IEEE Geosci Remote Sens Mag 9, 53–81. https://doi.org/10.1109/MGRS.2020.3019315.

Vivone, G., Garzelli, A., Xu, Y., Liao, W., Chanussot, J., 2023. Panchromatic and Hyperspectral Image Fusion: Outcome of the 2022 WHISPERS Hyperspectral Pansharpening Challenge. IEEE J Sel Top Appl Earth Obs Remote Sens 16, 166–179. https://doi.org/10.1109/JSTARS.2022.3220974.

Wang, Y., Zhu, Q., Shi, Y., Song, M., Yu, C., 2021. A Spatial-Enhanced LSE-SFIM Algorithm for Hyperspectral and Multispectral Images Fusion. Remote Sens (basel). https://doi.org/10.3390/rs13244967.

Wei, Q., Bioucas-Dias, J., Dobigeon, N., Tourneret, J.-Y., 2015. Hyperspectral and Multispectral Image Fusion Based on a Sparse Representation. IEEE Transactions on Geoscience and Remote Sensing 53, 3658–3668. https://doi.org/10.1109/TGRS.2014.2381272.

Yokoya, N., Grohnfeldt, C., Chanussot, J., 2017. Hyperspectral and Multispectral Data Fusion: A comparative review. IEEE Geosci Remote Sens Mag 5, 29–56. https://doi.org/10.1109/MGRS.2016.2637824.

Yuhas, R.H., Goetz, A.F., Boardman, J.W., 1992. Discrimination among semi-arid landscape endmembers using the spectral angle mapper (SAM) algorithm., in: Summaries of the Third Annual JPL Airborne Geoscience Workshop. Pasadena, California, USA, pp. 147–149.

Zhang, K., Zhang, F., Wan, W., Yu, H., Sun, J., Del Ser, J., Elyan, E., Hussain, A., 2023. Panchromatic and multispectral image fusion for remote sensing and earth observation: Concepts, taxonomy, literature review, evaluation methodologies and challenges ahead. Information Fusion 93, 227–242. https://doi.org/10.1016/j.inffus.2022.12.026.

Zitová, B., Flusser, J., 2003. Image registration methods: a survey. Image vis Comput 21, 977–1000. https://doi.org/10.1016/S0262-8856(03)00137-9.